AUTOMATED TESTING AND MACHINE-LEARNING-BASED MODELING OF AIR DISCHARGE ESD

BY

SAM SAGAN

THESIS

Submitted in partial fulfillment of the requirements
for the degree of Master of Science in Electrical and Computer Engineering
in the Graduate College of the
University of Illinois at Urbana-Champaign, 2017

Urbana, Illinois

Adviser:

Professor Elyse Rosenbaum

Abstract

An IEC 16000-4-2 compliant, high-accuracy air-discharge automation system is used to study the properties of air discharge *electrostatic discharge* (ESD). This work corroborates conclusions of previous works and presents new insights into the effects of approach speed on ESD. A methodology for machine-learning-based ESD modeling is presented. Models are validated with a high degree of accuracy against measurement data.

Acknowledgments

Contents

1. Introduction

This work aims to further the field of ESD through the use of a high-performance automation system and cutting-edge statistical learning methods. Previous works have studied the effects of approach speed of air discharge at speeds greater than 50 mm/s. This work studies the effects of speeds up to 50 mm/s over the full range of industry standard ESD precharge levels for air discharge. The automated system improves repeatability of IEC 16000-4-2 air-discharge testing and allows for precise control of approach speed.

A statistical learning method called naïve Bayes is applied to the problem of air-discharge ESD modeling. The model is trained on a dataset of 1375 measured waveforms and validated against another set of measurement data.

Figure 1 demonstrates that zaps to different locations on real equipment-under-test (EUT) exhibit vastly different discharges. These zaps were performed on a slider cell phone; however, this study uses a simpler target, with known geometry and electrical properties, that does not exhibit variability between zap points. One discharge waveform for the simple EUT is overlaid in Figure 1.

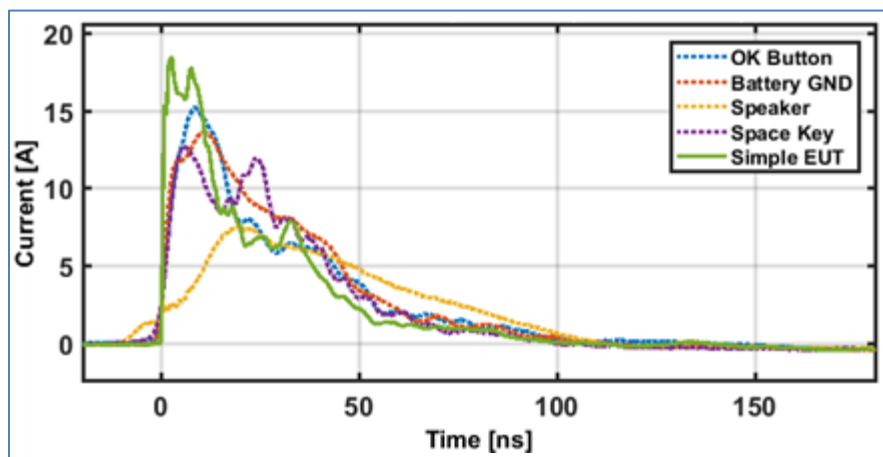**Figure 1. Varied zap locations on a real EUT demonstrate significant variability. A simpler EUT, described in Section 4, is used as the target in subsequent parts of this study.**

This work presents a methodology for modeling discharge parameters using naïve Bayes method. Samples from the model's output, a posterior joint *probability density function* (pdf), are compared to measurement data to validate the model.

2. Previous Work

Researchers have approached air discharge measurement and modeling in a variety of ways. Previous works indicate that air electrostatic discharges are not highly repeatable [1], [2]; this is confirmed by the measurement data plotted in Figure 2. Controlling the test conditions reduces, but does not eliminate, variance in measured discharge waveforms. Discharges from an IEC 16000-4-2 air discharge gun tip to a target with matching spherical curvature are optimally reproducible [3], [2], [4]. However, the geometry of the matching target, shown in Figure 3, is not representative of most EUT. Thus, researchers must accept non-optimal air-discharge reproducibility when working with realistic EUT, such as consumer products.
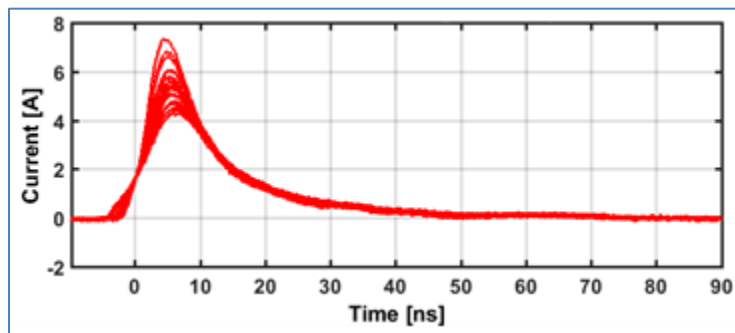
Figure 2. 25 Overlaid air discharges demonstrate the inherent variability of air discharge ESD. These discharges are performed at 15 kV on the simple EUT described in Section 4 with an approach speed of 15 mm/s.
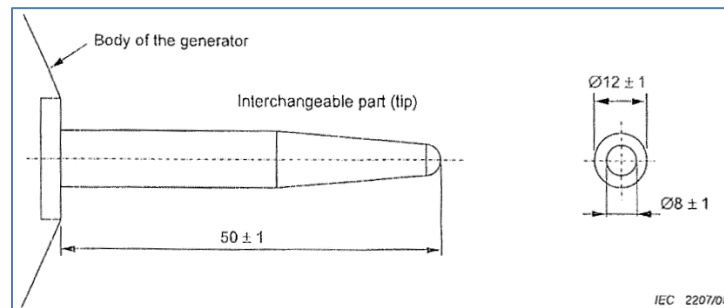
Figure 3. The IEC 16000-4-2 standard air-discharge gun tip produces optimally repeatable discharges when the target is of the same geometry [3].

As it cannot be eliminated in practice, air discharge variability must be minimized. Experimenters build machines to precisely control the motion of the ESD gun or charged electrode. Three such designs are diagramed in Figure 4, Figure 5, and Figure 6. These machines improve the reproducibility of the discharge while allowing researchers to explore the effect of approach speed on the discharge. In this work, an IEC 16000-4-2 compliant machine described in Section 3 mechanically controls the testing. The

machines used in previous works do not comply fully with the IEC standard because their EUT are not positioned on the horizontal coupling plane of an IEC 16000-4-2 testbed, defined in Appendix A.
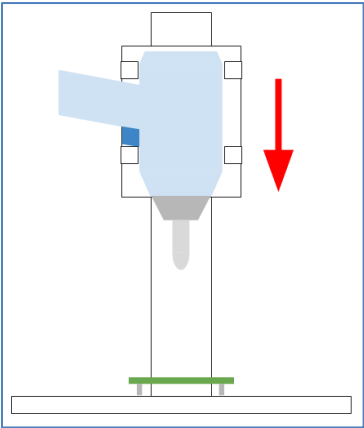
Figure 4. Vertically driven gun mount for motion on the order of a few mm/s [2]
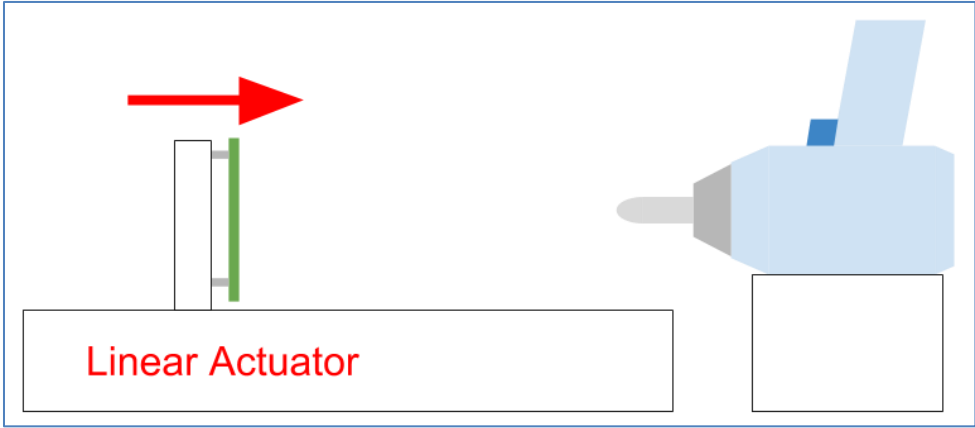
Figure 5. Horizontally driven target reaching speeds of 200 mm/s from [4]
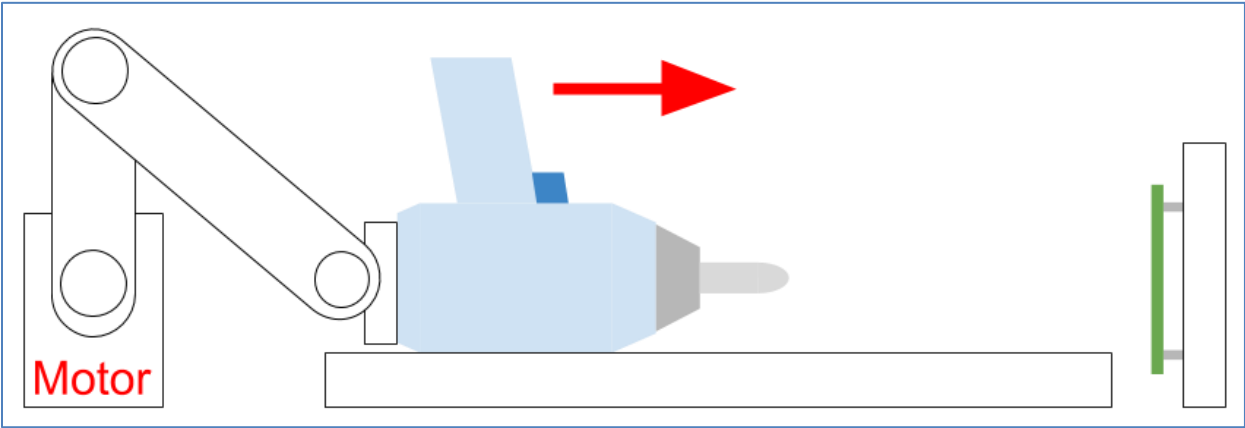
Figure 6. Horizontally driven ESD gun reaching speeds of 500 mm/s from [5]

Various works have studied the effects of approach speed on discharge waveforms. For a fixed precharge voltage, spark length decreases with greater approach speed, and a shorter spark length corresponds to faster rise-time [4], [6]. Theoretical analysis suggests that high approach speeds or decreased ambient air pressure correlate to higher peak current as well [7]. An empirical expression relating the peak discharge current and rise-time to the precharge voltage was proposed in [8]; the equation is given in (2.1) where α is a fitting parameter that varies with gun approach speed, ambient temperature, and humidity. Figure 7 demonstrates that (2.1) is consistent with the data obtained in this work.

$$\frac{I_{peak}}{V_{pre}} = .002t_r^{-\alpha} \tag{2.1}$$
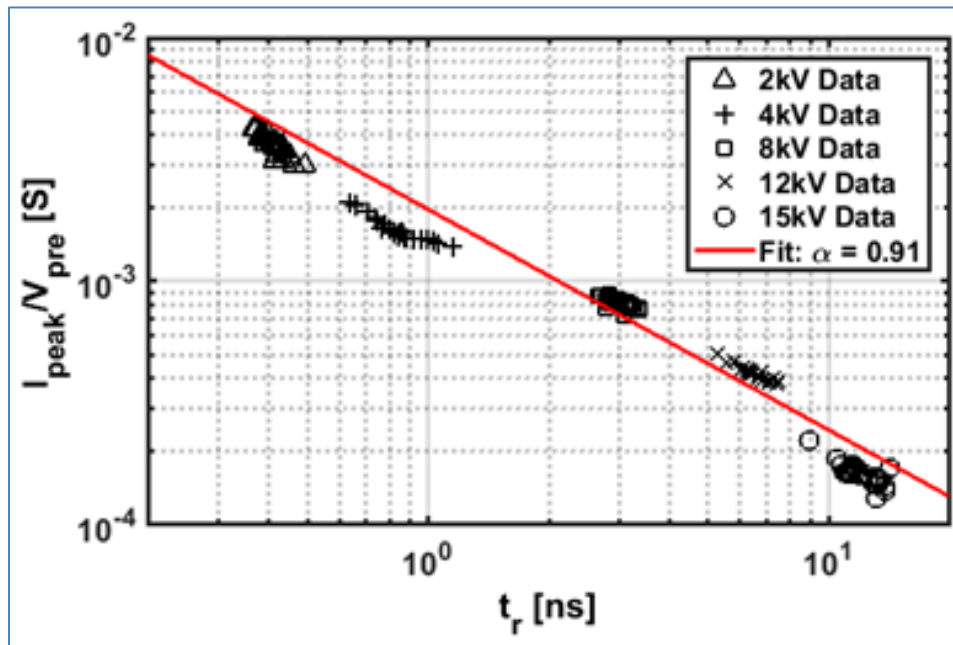
Figure 7. Equation (2.1) fits with a high degree of accuracy to data obtained in this study, corroborating the previous work of [8]. Data are obtained using the simple EUT described in Section 4 with an approach speed of 35 mm/s.

The observable spark during air discharge ESD is a complex and highly nonlinear effect which previous works have modeled in various ways. Bernoulli's equation relating air pressure to kinetic and potential energy has been used alongside Townsend's equations for breakdown of gases to explain some of the effects of high approach speed [7]. The Rompe-Weizel spark resistance formula and full-wave electromagnetic solvers have been used in conjunction to model the time-varying resistance of the spark [6].

Some works debate the usefulness of air discharge due to its limited reproducibility [1], [2]. The IEC 61000-4-2 Standard, however, defines the air discharge procedure such that it best models real-world ESD between a charged human holding a conducting object and an EUT. Proposing an alternative to air discharge, some researchers showed that contact-mode discharges through a fixed air gap are less variable than traditional air discharge; however, the proposed method does not model real-world ESD as precisely [1]. This does not imply that changes to the test standard should not be considered; for example, the growing wearables market may warrant modifications to the IEC 16000-4-2 Standard. Human interactions with wearables are poorly modeled by the standard with the most severe wearable discharges occurring when a body-mounted device on a charged human comes in contact with a grounded conductor [9]. It has been observed that such discharge waveforms have significantly higher peak currents than those outlined in the IEC 16000-4-2 Standard [9].

3. Automated Air Discharge Tester

To improve the reproducibility of air discharge testing in this work, an electromechanical system moves the ESD gun towards an EUT at precise speeds. The system, diagramed in Figure 8, includes features to automate air discharge testing as well.
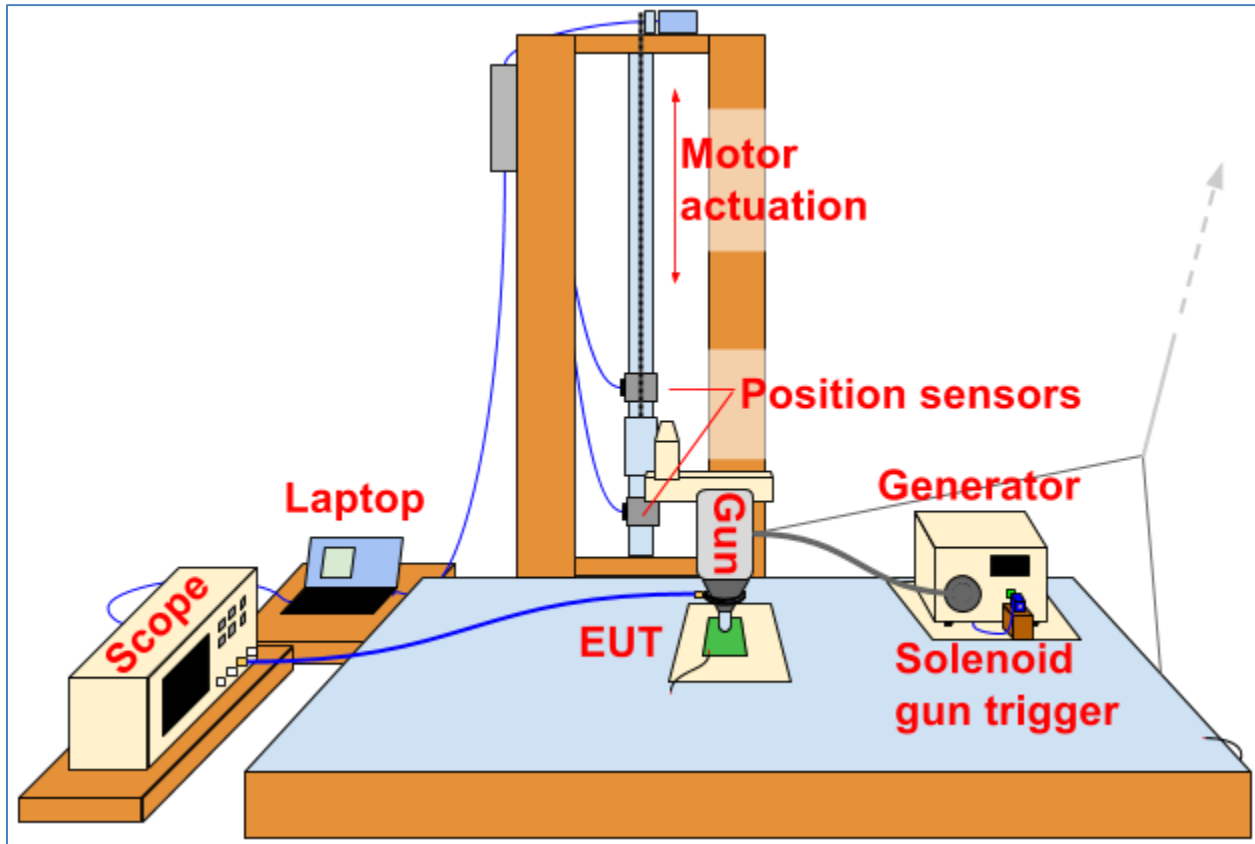
Figure 8. Automated tester diagram. A motor drives an adjustable gun-mounting arm up and down over an EUT. Position sensors track the location of the arm, and a solenoid pushes the gun-trigger button on the ESD generator. An oscilloscope measures discharge waveforms, and the system is controlled by a laptop.

3.1 Features

The system provides precise velocity control at up to 50 mm/s. Controlled by a computer, the tester can execute and record results from an array of tests without human interaction. Using the system, it took approximately 8 hours to record 1775 waveforms comprising the training and validation datasets used in this study. The gun's contact location on the EUT is manually adjustable. Unlike the previously described systems in [2], [4], and [5], this one is IEC 16000-4-2 compliant because it zaps EUT on the standard testbed detailed in Appendix A: The IEC Testbed.

3.2 Electromechanical Design

A wooden tower stands on the floor behind the ESD testing table. A mechanical arm, consisting mostly of insulating material, extends from the tower over the center of the testbed. The ESD gun is fixed onto the arm such that the electrode is positioned precisely perpendicular to the tabletop.

The tower has a sprocket and chain system that raises and lowers the gun-carrying arm. A geared stepper motor drives the system at 11.1 µm of linear motion per full-step. The sliding mechanism consists of aluminum extrusion and a mechanical slide.

In order to automate the testing procedure, a solenoid actuator triggers the ESD generator at the beginning of each test. To maintain precise vertical positioning above the EUT and prevent damage to the system, the arm has position sensors mounted above and below it—both adjustable.

3.2.1 Chain Drive System

The drive system consists of a motor, chain, and sprockets; it is responsible for raising and lowering the arm with precise positioning and speeds up to 50 mm/s. Figure 9 depicts the driver sprocket (in red) pulling a chain around two idler sprockets (in blue) to raise and lower the arm. The driver sprocket is mechanically fixed to the motor shaft whereas the idler sprockets spin freely on low-friction bearings.
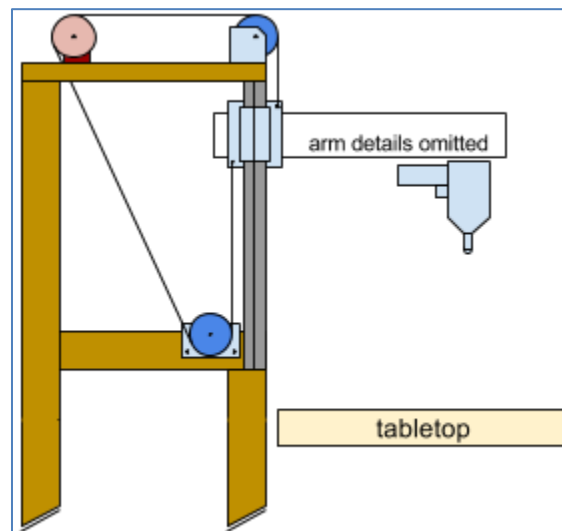
Figure 9. The existing mechanical drive system includes a closed chain loop around a driver sprocket (red) and two idler sprockets (blue).

This is the second iteration of this drive system's design. The first did not consist of a closed chain loop; rather, it raised the arm at one end and carried a counterweight on the other, as seen in Figure 10. The slider connected to the arm that moves along the vertical aluminum bar has low, but non-zero, friction. The weight of the arm places a torque on the slider and causes increased friction forces which impeded

the downward motion propelled by gravity. Thus, when lowered at above 5 mm/s, slack would appear in the chain, and the arm would fall at a rate slower than desired. Closing the mechanical loop so that the motor also pulls the arm down fixed this problem. Notably, the final design requires a motor with more torque than the original due to the elimination of the counterweight.
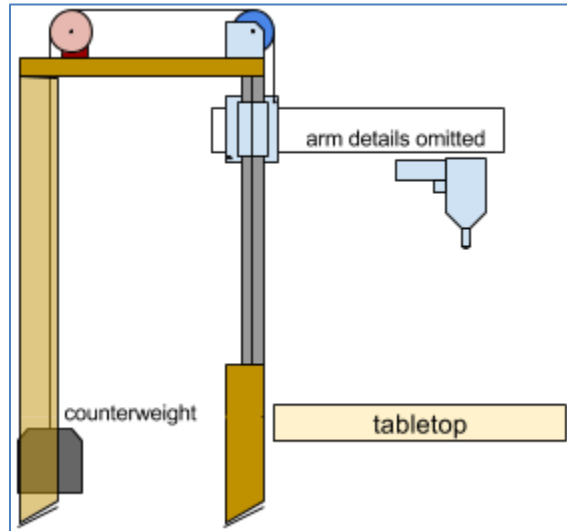
Figure 10. The original counterweight-based mechanical drive system included an open chain loop.

3.2.2 Motor Selection

The chosen motor ensures that the accuracy of the vertical positioning of the arm is within 0.5 mm. This is a reasonable amount of error to ensure that the gun makes contact with the EUT without breaking it. As the gun contacts the EUT, the arm can bend slightly, relieving some pressure on the EUT and preventing the powerful motor from breaking the EUT with the gun tip.

The motor must have sufficient torque to accelerate the arm upward to a maximum linear speed of 50mm/s without losing positional accuracy. The motor experiences peak torque while moving the arm upward to its starting position following contact with the EUT because the motor must lift against the force of gravity. Figure 11 is a free-body diagram of the arm during upward acceleration, where the forces are governed by (3.1). Assuming a constant rate of acceleration (a), (3.2) gives the amount of time necessary (Δt) to accelerate to maximum speed from rest. Note that the force due to friction is ignored for simplicity, so this calculation underestimates Δt.

$$ma = F_{motor} - mg \qquad (3.1)$$

$$\Delta t = \frac{\Delta v}{a} \qquad (3.2)$$

8
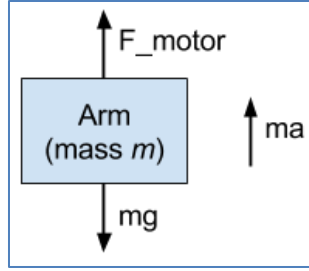
Figure 11. A free-body diagram of the arm as it is accelerated upward by the motor. The forces are mathematically governed by equation (3.1).

The geared stepper motor has a holding torque of 40 newton-meters (N·m). Holding torque is a metric that applies only to the motor at low step rates—non-idealities decrease the torque at higher step rates. The arm has a mass of 4.35 kg, and the driver sprocket has a *pitch diameter* (PD) of 1.282 inches (32.56 mm). The pitch diameter is defined in Figure 12 and is twice the radius (r). Per equation (3.3), the motor can provide a linear force of 2457 N at low speeds, which far exceeds the gravitational force of the arm (43 N).

$$Force = \frac{\tau\ (torque)}{r\ (radius)} = \frac{2\tau}{PD} \tag{3.3}$$
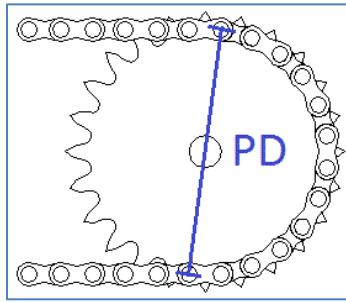
Figure 12. The pitch diameter (PD) of a sprocket is measured between the centers of opposite chain rollers.

Parasitic non-idealities in the motor cause an increased step rate to decrease torque. The coil current must rise and fall once to complete a full step, and the coil current rise-time is finite. The motor is rated for a peak coil current of 3.96 A and powered by a 48 V supply. The reported coil resistance is 0.9 Ω, and the inductance is 2.5 mH. Per (3.4), the coil current rise-time (t_{r-coil}) to 3.96 A is 272 µs.

$$I(t) = \frac{V}{R}\left(1 - e^{-t\frac{R}{L}}\right) \tag{3.4}$$

Assuming the rise- and fall-times to be equal, a full-step requires twice t_{r-coil}, and the maximum full-step frequency ($f_{\tau-max}$) at which the motor can maintain maximum torque is given by (3.5) and evaluates to 1838 Hz.

$$f_{\tau-max} = \frac{1}{2t_{r-coil}} \tag{3.5}$$

9

The linear velocity of the arm is related to the step frequency by (3.6). Given that the motor's gear ratio is 46.656:1 and the shaft before gearing takes 200 steps per rotation, the total number of steps per rotation is 200 times the gear ratio. A 1838 Hz step rate corresponds to a linear arm speed of 20.2 mm/s. Since the system must operate at up to 50 mm/s, the motor will have to operate under conditions of decreased torque.

$$v = f \frac{\pi * PD}{200 * ratio} \tag{3.6}$$

At 50 mm/s, equation (3.6) gives that the motor must run at a step frequency of 4561 Hz. At this frequency, the coil current will not reach its peak value; rather, it will reach 1.64 A, per (3.4) and (3.5). Since torque is proportional to electrical power, it varies with the square of the coil current. If 3.96 A peak current corresponds to 40 N·m torque, then 1.64 A corresponds to 6.86 N·m, or a linear force of 421 N. Revisiting kinematic equations (3.1) and (3.2) at this linear force, the time it would take to accelerate the mass of the arm upward against gravity to 50 mm/s is 575 μs. This is the time of about 2.1 full-steps. During these steps, the shaft step-rate will not match the desired step-rate and the shaft's motion is not well defined. This means that the theoretical error in the positional accuracy of the system is about 3 full-steps, or 32.99 μm, per (3.7).

$$d = steps \frac{\pi * PD}{200 * ratio} \tag{3.7}$$

This error does not affect the approach speed's accuracy since the motor only sees overwhelming torque while accelerating the arm up to speed—not while moving at a constant rate.

3.2.3 Stepper Motor Driver
The DM542T stepper motor driver generates the current waveforms that control the motor shaft. This driver takes in a DC voltage of up to 50 V and outputs peak coil currents of up to 4.2 A. The DM542T cuts the coil current by half when the motor is stationary. Per the torque calculations in section 3.2.2, this is still more than enough current to hold the arm stationary.

3.2.4 Solenoid Actuator
The solenoid actuator presses the gun-trigger button on the ESD generator. The solenoid is mounted on a wooden stand that can be attached and detached from the ESD generator.

3.2.5 Position Sensor Mounting
There is a photointerrupter mounted above and below the mechanical arm. These photointerrupters have a sensing distance of 15 mm, which is appropriate for catching the exposed section of the arm's slider (10 mm thickness). The top sensor is mounted on another slider with a mechanical brake such that

the user can quickly and easily lock it at the calibration height. Figure 13 demonstrates the position at which the electrical-tape-covered corner of the arm slider trips the sensor.
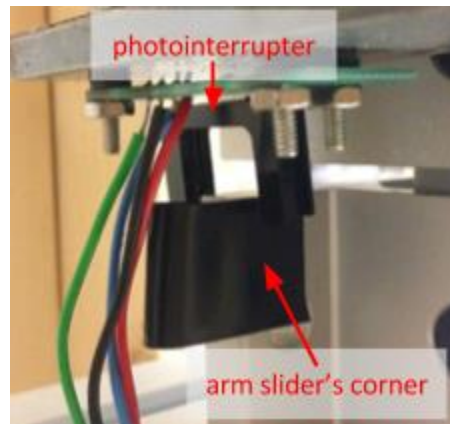
Figure 13. The top position sensor is mounted on a slider above the arm's slider. This image depicts the position at which the electrical-tape covered corner of the arm slider trips the photointerrupter.

The bottom sensor should be adjusted such that it will trip if the arm moves a millimeter or two further down than the point at which the gun contacts the EUT. Again, note that upon contacting the EUT, the arm can bend slightly, which prevents the motor from breaking the EUT with the gun tip. The user should adjust this bottom sensor every time a new EUT is placed under the gun. Adjustments are made by loosening the bolt that keeps the sensor's mounting block in place.

3.3 Electrical Control System and Power

A PIC16f887 microcontroller communicates with the computer through a USB interface IC. Further, it takes in readings from the two photointerrupter circuits. The microcontroller sends control signals to a stepper motor driver and a transistor controlling the solenoid actuator. The computer controls the oscilloscope and receives waveform data through a GPIB connection. The system is powered by a 10 A, 48 V AC/DC converter.
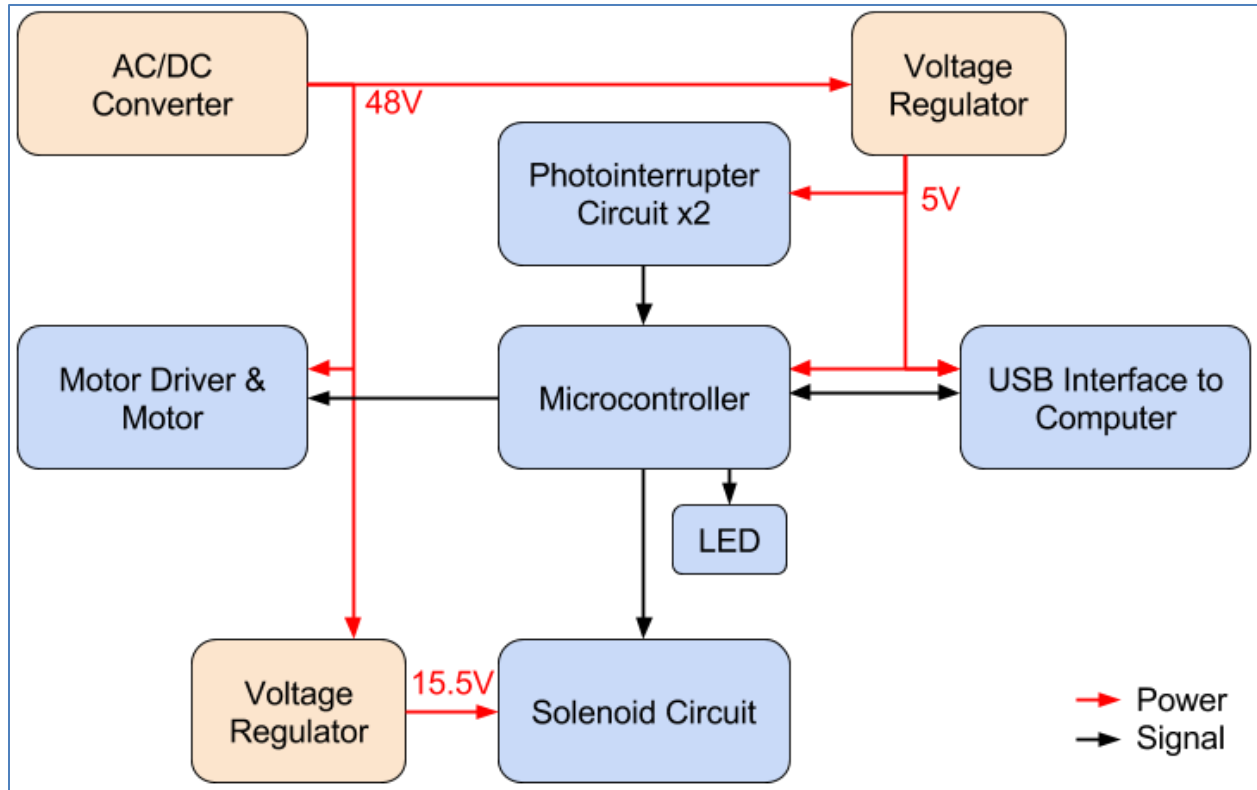
Figure 14. Electrical block diagram

3.3.1 USB Interface

A FT245RL USB interface IC manages the USB connection and converts serial data on the computer's side to 8-bit parallel data on the microcontroller's side and vice versa. An interrupt-based communication scheme that includes instructions and handshakes was developed between the computer and microcontroller. The instruction set includes running an experiment, manually adjusting the arm, calibration, and stopping the system. Distances and speeds must be sent back and forth in units of steps and steps/s, respectively. Both are encoded with 3 bytes transmitted over USB, which is sufficient to represent every value the system must communicate.

3.3.2 Motor Control

The microcontroller sends three signals to the stepper motor driver: step, direction, and enable. All three are configured to be active high. The step signal consists of a square wave, and each rising edge corresponds to a step of the motor. The step signal is implemented using the Capture/Compare/PWM module of the microcontroller in compare-mode instead of PWM-mode. Pulse-width modulated (PWM) signals are a natural choice for producing a step signal; however, the compare module can be configured to produce a wider range of step frequencies. While PWM-mode would have allowed variability in the duty cycle, this is unnecessary for controlling a stepper motor. The direction signal takes on either a high

or low logical value with a high corresponding to raising the arm, and a low, to lowering it. The enable signal is high when the system is on.

3.3.3 Solenoid Control

The microcontroller outputs a single logical signal to engage or disengage the solenoid. Figure 15 depicts a schematic for the drive circuity of the solenoid. A logical high allows current to flow through the solenoid, engaging it and pressing the gun-trigger button. The diode protects the transistor from *flyback*—the voltage spike produced when the current through an inductive load suddenly changes. The supply voltage was tuned to be minimum such that the solenoid would still maintain enough linear force to press the gun-trigger button. Minimizing this voltage decreases the current through the solenoid and lowers the heat dissipation of the solenoid's voltage regulator. The transistor can also become hot while the solenoid is engaged, so it is heatsinked.
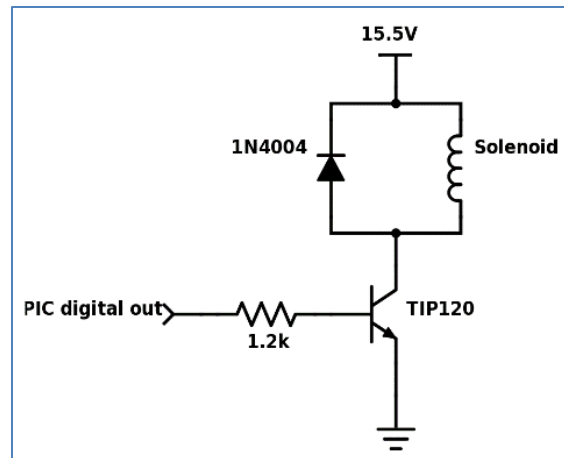

Figure 15. The solenoid circuitry actuates the device when a logical high is applied.

3.3.4 Position Sensors

A photointerrupter is a combination of an LED emitting in the non-visible range and a phototransistor that conducts current when exposed to the LED's light. The circuit in Figure 16 generates a logical low when the photointerrupter is tripped and a high otherwise.
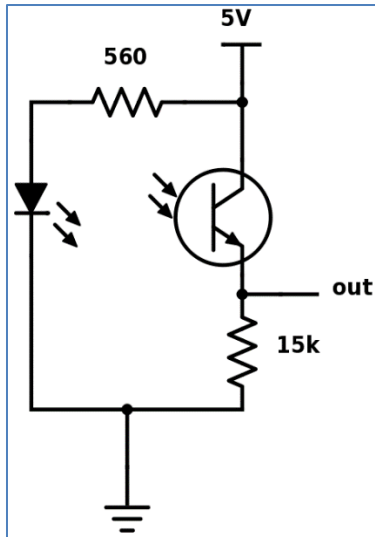
Figure 16. The photointerrupter circuit (position sensor) produces a logical low when tripped.

The photointerrupters protect the system in the cases of user error or electromagnetic interference (EMI) related system failure. The motor is powerful enough to break the tower or an EUT if it were to run continuously upward or downward. To avoid this, the microcontroller checks the state of the sensors before any step is taken and stops the motor if a sensor trip occurs outside of normal operation. Normal operation includes returning to the position of the top sensor after every zap; thus, any trip of the bottom sensor or any other trip of the top sensor will stop the motor. Identifying whether a trip of the top sensor is part of normal operation or otherwise is handled by a state-machine coded on the microcontroller.

An indicator LED is turned off whenever either of the sensors is tripped and on otherwise. The operator will use this LED during calibration.

3.3.5 Power

A 48 V, 10 A AC/DC converter powers the system. This is regulated down to 15.5 V for the solenoid actuator and 5 V for the microcontroller and USB interface IC. The power dissipated by a voltage regulator as heat is given by (3.8). Decreasing current through the regulators decreases heat dissipation. The solenoid draws about 100 mA when engaged, and the 5 V domain draws about 50 mA. Both regulators have internal thermal shutoff circuitry, but using two heatsinks on each keeps them within safe operating conditions.

$$P_d = (V_{in} - V_{out})I \tag{3.8}$$

3.3.6 EMI Mitigation

Triggering the ESD generator produces a large amount of electromagnetic noise that can interrupt the operation of the control system. The current implementation of the system may fail due to EMI once in every 20 to 50 zaps of the ESD gun at precharges between 8 and 15 kV. Such failures cause the microcontroller code to hang and can only be recovered by power-cycling the automated tester's control system. Interruptions were more frequent before eliminating a large ground loop and adding shielding. Figure 17 diagrams the connections and shielding in the system. The control circuits themselves are housed in a shielded box. All shielded connections consist of 22-gauge wire twisted together and shielded with a tight layer of aluminum foil. Ensuring a reliable ground over the complete length of the shield is important for minimizing electromagnetic susceptibility and can be achieved by grounding the shield at both ends with short wire connections. In the case of the motor and solenoid leads, the wires do not carry a system ground so the shield cannot be grounded at the motor or solenoid. The solenoid connection is especially susceptible to EMI due to its close proximity to the ESD generator. In an attempt to ground the solenoid end of that shield, a connection was made directly to the building ground (the dashed line in Figure 17); however, this was removed because it introduced a ground loop that increased electromagnetic susceptibility.
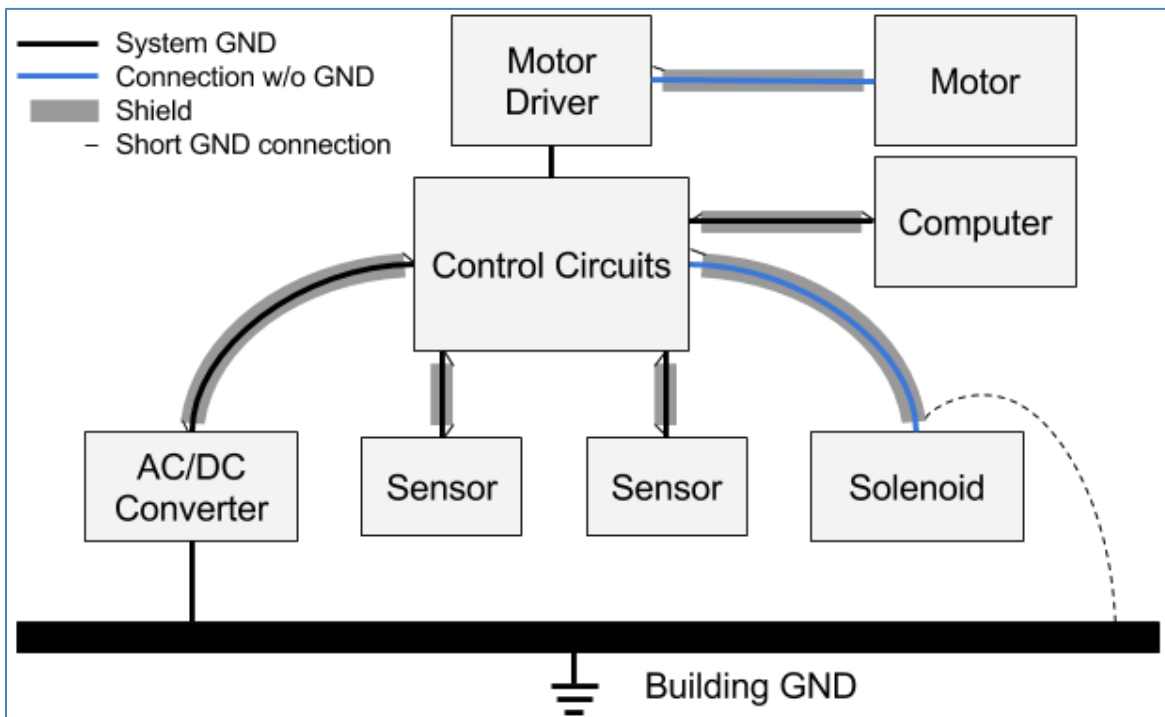
Figure 17. Long wire connections are shielded. A connection that includes system ground (black lines) can be used to ground the shield at both ends with short wires; however, connections without ground (blue lines) cannot. The dashed line represents an attempt to ground the end of the especially long solenoid connection; however, it was removed because it created a ground loop.

3.4 User Interface

The graphical user interface (GUI) allows the user to perform calibration and input the test parameters such as trigger height and approach speed. The main window of the GUI is included in Figure 18.
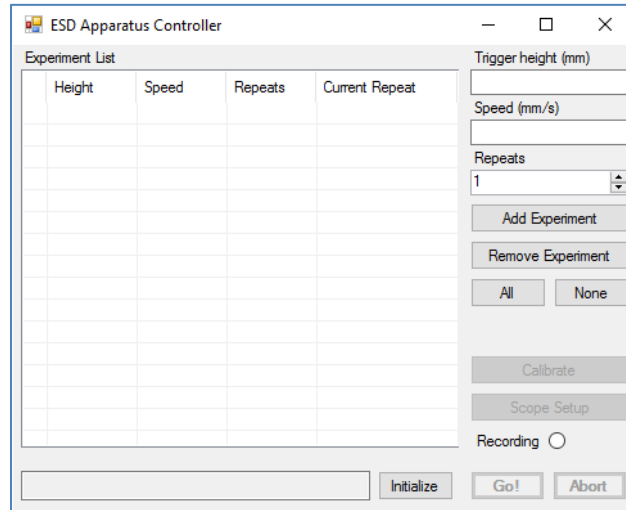
Figure 18. The main window of the GUI. The user may perform calibration and input test parameters such as trigger height and approach speed.

Every experiment consists of the gun moving downward from the calibration height, triggering the ESD generator at a prescribed trigger height, contacting the EUT, and returning to the calibration height (see Figure 19). All this is done at a given approach speed.
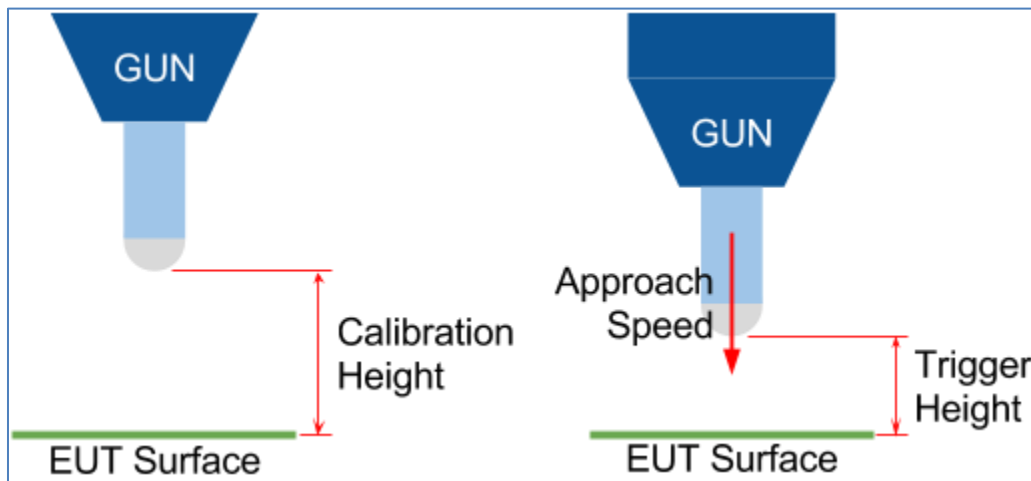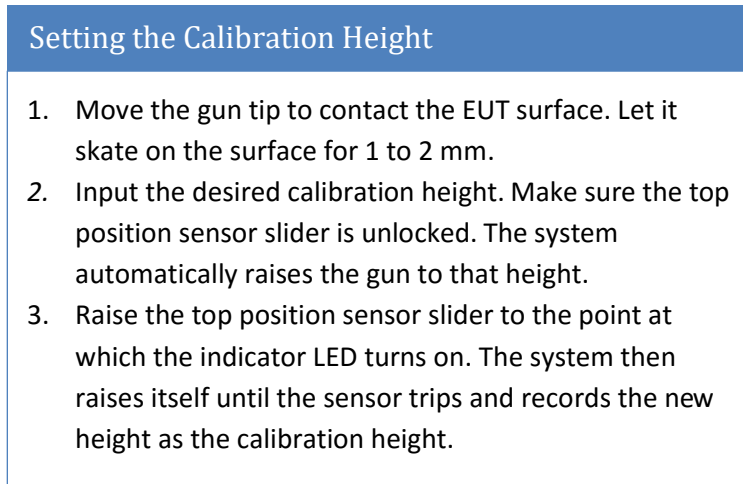
Figure 19. At the beginning of an experiment, the gun begins moving downward from the calibration height (left). As it moves downward at a specified approach speed, the ESD generator is triggered at the specified trigger height (right).

Before testing, the user must perform the calibration procedure in Figure 20 for setting the calibration height.

Setting the Calibration Height

1. Move the gun tip to contact the EUT surface. Let it skate on the surface for 1 to 2 mm.
2. *Input the desired calibration height. Make sure the top position sensor slider is unlocked. The system automatically raises the gun to that height.*
3. Raise the top position sensor slider to the point at which the indicator LED turns on. The system then raises itself until the sensor trips and records the new height as the calibration height.

Figure 20. Procedure for setting the calibration height

4. Data Acquisition and Processing

The ESD generator is a Noiseken ESS-B3011 with a Noiseken GT-30R ESD gun. The target is an FR4 board with 1 oz. copper on both sides as seen in Figure 21. The sides are shorted together using conducting tape along the perimeter. The dimensions of the board are 117 mm x 54 mm raised with non-conducting standoffs such that the zap point is 20 mm above the horizontal coupling plane (HCP). The EUT surface is resistively tied to the HCP through a 940 MΩ resistor which allows the target to discharge between zaps. Note that the large resistance bleeds charge off the target on a much slower timescale than that of the ESD.
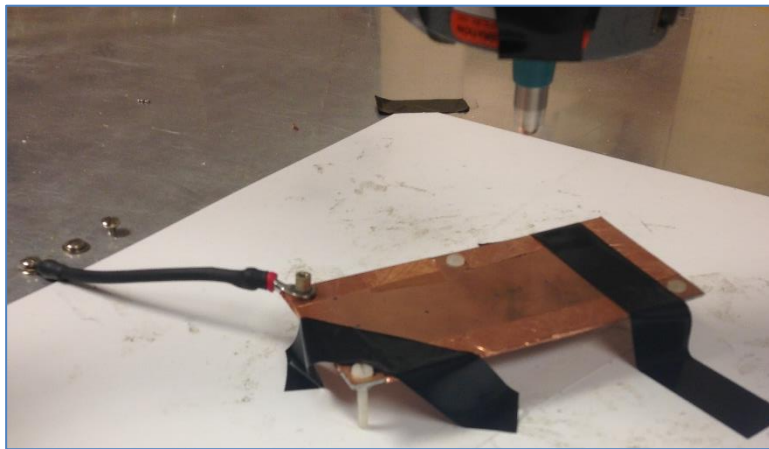
Figure 21. The target in this study is an FR4 board with 1oz copper on both sides taped to an insulating sheet and resistively tied to HCP.

For the model training dataset, the precharge voltage and approach speed are varied. Precharges of 2, 4, 8, 12, and 15 kV; and speeds of 1, 5, 10, 15, 20, 25, 30, 35, 40, 45, and 50 mm/s are used. The industry standard precharge voltages for air discharge testing are all those above besides 12 kV [3]; however, 12 kV is included to eliminate the large gap in training data between 8 and 15 kV which would likely limit the ability of the model to interpolate precharge voltages in that gap. The set of approach speeds was chosen to cover the range of interest without leaving gaps or distributing the training data non-uniformly. Non-uniformity in the training data can lead to undue bias in the model. 25 discharges are recorded at each combination of precharge and speed.

The first step in processing a discharge consists of parsing the output file from the oscilloscope. Next, the waveforms are filtered with a 1 GHz bandwidth, fourth-order Butterworth low-pass filter. At this cutoff frequency, the current probe's frequency response drops 1 dB below the passband value. Thus, any artifacts of that drop-off will be attenuated by the filter. A Butterworth filter is used because it has no ripple in the passband and thus avoids altering the passband frequency content of the data.

As defined in Figure 22, peak current, total charge dissipation, and rise-time are then extracted from each waveform. It is hypothesized that these three output variables are key predictors of soft and hard failures due to ESD. In the future, the automated tester can be used to test this hypothesis. A soft failure is a recoverable disruption most likely caused by a fast rise-time and high peak current. Hard failures are characterized by devastating damage to a device due to Joule heating which prevents normal operation indefinitely—they are likely correlated with the total energy of the discharge given by (4.1). However, this energy calculation cannot be completed because the EUT's impedance at the zap location and the resistance of the spark are not measured in this work. Total charge is correlated to total energy and can be calculated by simply integrating the current waveform as shown in (4.2).

$$E_{tot} = \int_{t_0}^{t_{end}} I^2 R\, dt \tag{4.1}$$

$$Q_{tot} = \int_{t_0}^{t_{end}} I\, dt \tag{4.2}$$

Extracting peak current and total charge are accomplished by taking the maximum and trapezoidal sum of the discharge waveform, respectively. Extracting rise-time requires interpolation of the waveform's discrete points on the rising edge.
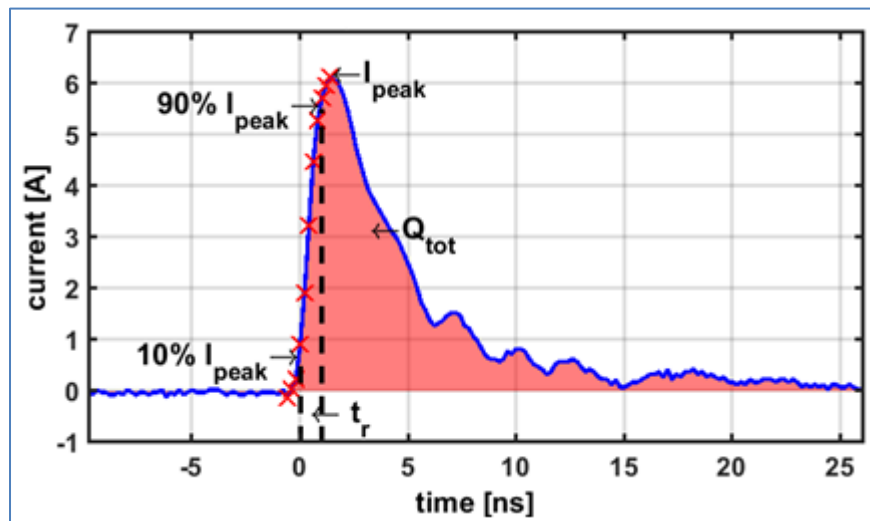
Figure 22. Waveform metrics. Q_{tot} is the total charge (the red area under the curve). I_{peak} is the peak current. Rise-time is measured from the time at which the current rises to 10% of the peak value to the time at which it rises to 90%.

When acquiring waveforms, it is important to adjust the time axis of the oscilloscope to maximize the sample rate by ensuring that the discharge waveform fills the scope's screen. Further, the vertical axis should be adjusted to use the smallest volts-per-division without clipping the waveform. This way, the oscilloscope's analog-to-digital conversion (ADC) has the finest possible discretization. Increasing the

frequency of samples and using the smallest ADC discretization improves the accuracy in extracting waveform parameters.

It is important to note that the current probe has zero coupling at DC. This has a significant effect on the waveforms which can be seen in Figure 23. This effect is small when measuring rise-time or peak current, but has a noticeable effect when integrating the waveform to calculate total charge dissipation. It is impossible to recover the DC level of the signal because it is at the null of the probe's frequency response. This causes all subsequent total charge calculations to underestimate the true charge dissipation. However, inverse filtering to eliminate the high-pass response may reduce the measurement error.

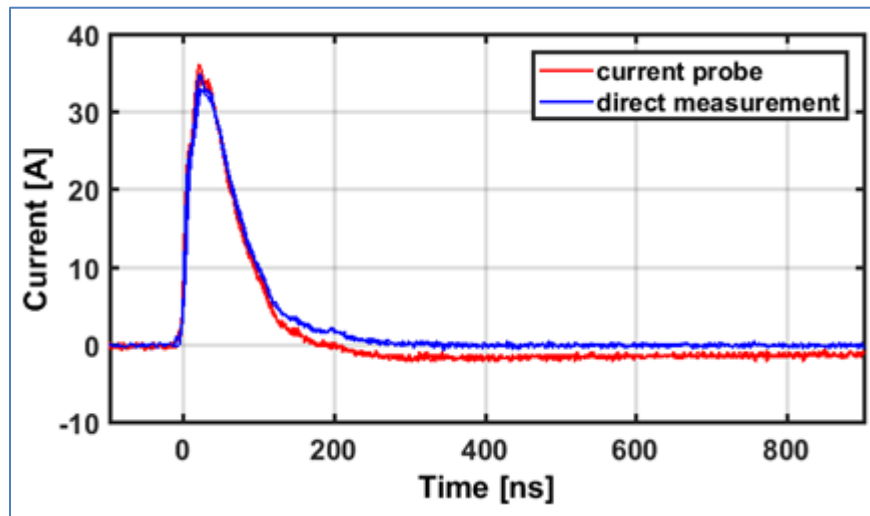**Figure 23. The current probe blocks DC signals which causes its measurements to underestimate the total charge entering the EUT. The plot depicts overlaid waveforms of air discharges to a 2 Ω target which has an SMA connection that allows for direct measurement of the discharge current.**

5. Measurement Results

Previous works indicate that as the approach speed is increased, the discharge's peak current increases and its rise-time decreases [4], [6], [7]. However, the studies used approach speeds that were greater than 50mm/s. This work investigates the effect of approach speeds up to 50 mm/s.

Secondary discharges following the initial spark are observable for precharge levels of 4 kV or higher. This phenomenon is documented in section 5.4. For each approach speed, the trigger height and oscilloscope *holdoff* settings are carefully chosen to guarantee that the scope acquires only the first discharge. The oscilloscope holdoff sets the amount of time that acquisition is disabled following a scope trigger event. The holdoff must be greater than the amount of time from the initial discharge to contacting the EUT to avoid acquiring any secondary discharges. At the same time, the scope registers a trigger event every time the ESD generator is triggered with the solenoid. Thus, the amount of time between triggering the ESD generator and the first discharge must be greater than the holdoff.

Since the 15 kV discharge has a longer spark length than discharges of lower precharge voltages, setting holdoff and trigger height to capture the initial discharge at 15 kV will guarantee acquisition of the initial discharge at lower precharges. Further, increasing the trigger height always makes it easier to acquire the initial discharge; however, increasing trigger height causes experiments to take more time, especially at low approach speeds.

The calibration height must be set at or above the trigger height and must be large enough to guarantee that there is no mechanical oscillation in the gun tip when it discharges to the EUT. These oscillations could otherwise vary the zap location on the EUT by up to about 5 mm at 50 mm/s. These oscillations arise when the automated tester starts moving the gun from rest, but they are only appreciable at approach speeds greater than about 25 mm/s. At speeds 40 mm/s and higher, the oscillations are especially large, so during testing the calibration height was raised above the trigger height.

Following the guidelines in this section, experimental settings were chosen for each approach speed and reported in Table 1.

Table 1. Experimental settings for each approach speed

Approach Speed [mm/s]	Trigger Height [mm]	Calibration Height [mm]	Holdoff [s]
1	10	10	4
5	10	10	1
10	50	50	.7
15	50	50	.7
20	50	50	.7
25	50	50	.7
30	50	50	.7
35	50	50	.7
40	50	75	.7
45	50	75	.7
50	50	75	.7

5.1 Peak Current

Figure 24 shows that there is a positive correlation between approach speed and peak current for discharges at 2, 4, and 8 kV. However, at 12 and 15 kV, the peak current is relatively insensitive to approach speed, at least for speeds up to 50 mm/s. The non-monotonicity of the peak currents for discharges at 4 kV precharge voltage may be erroneous and due to an unreliable connection in the measurement equipment; however, it is recommended that further experiments be performed to assess the validity of the 4 kV data.
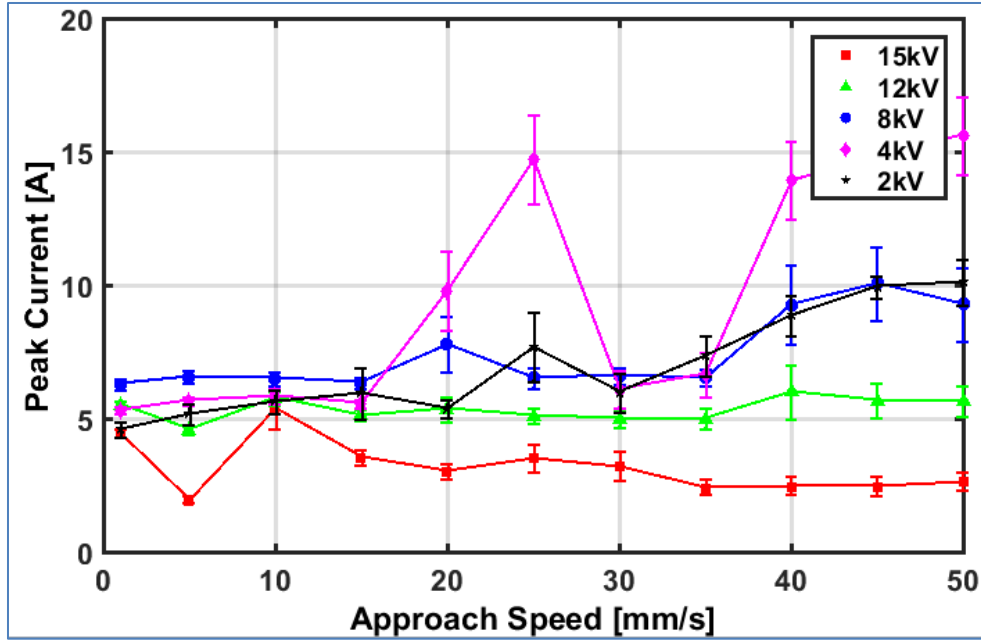
Figure 24. There is a positive correlation between approach speed and peak current for discharges at 2, 4, and 8 kV. At 12 and 15 kV, the peak current is relatively insensitive to approach speeds in this range.

5.2 Total Charge

As seen in Figure 25, there is a positive correlation between total charge and precharge voltage. The observed relationship can be explained using the ESD generator and gun model in Figure 26. Prior to triggering, the high voltage supply charges the storage capacitor through the charge relay switch. Upon triggering, the charge relay switch opens, leaving the charged storage capacitor to discharge through the discharge relay switch into the EUT. For a capacitor, $Q = CV$, so the amount of charge on the storage capacitor prior to discharge is proportional to the precharge voltage. The EUT and the horizontal coupling plane can be approximately modeled as a parallel-plate capacitor, and upon discharge, charge-sharing occurs between the storage capacitor and capacitive EUT.

Figure 25. There is a positive correlation between total charge and precharge voltage.
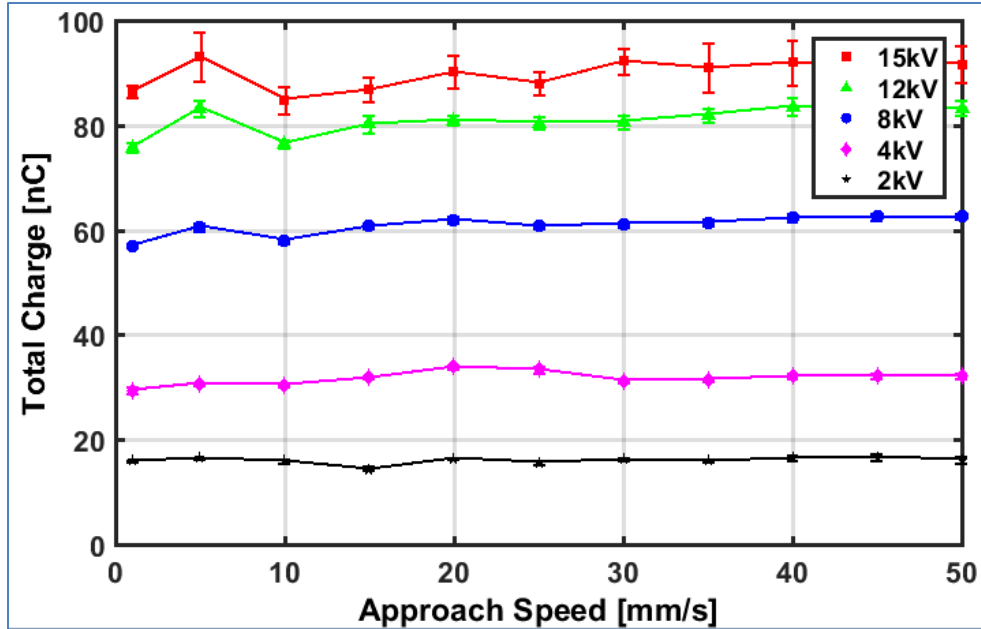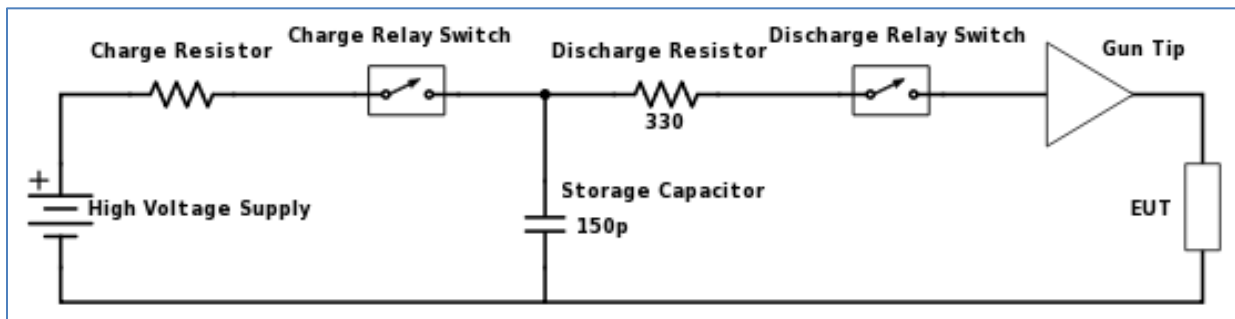

Figure 26. While triggered and approaching an EUT, the high voltage supply is off, and charge on the storage capacitor leaks through the charge relay switch, decreasing the amount of charge discharged during ESD [10].

For discharges at 8, 12, and 15 kV precharge, there is an observable non-monotonicity in the relationship between approach speed and total charge, with the latter peaking at 5 mm/s. Charge bleeds off of the storage capacitor through the open charge relay switch while the gun is triggered. Thus, a longer duration of gun trigger prior to discharge correlates with a lower total charge.

As reported in Table 1, the trigger heights for the experiments performed at 1, 5, and 10 mm/s are 10, 10, and 50 mm respectively. Recall that acquisition of the primary discharge necessitates these settings. Define *trigger-time* as the amount of time between triggering the gun and the initial discharge. The storage capacitor bleeds through the charge relay switch during this time; thus, the total charge decreases with increased trigger-time. Given the experimental parameters for approach speed and

trigger height, the trigger-time for the 5 mm/s test is shorter than for the 1 or 10 mm/s tests. This explains the peak in total charge seen at 5mm/s for discharges with 8, 12, and 15 kV precharge.

Again, as seen in Table 1, the trigger height of experiments with approach speeds between 10 and 50 mm/s is 50 mm. Thus, as the approach speed increases, the trigger-time decreases, and there is a slight increase in total charge for discharges with 8, 12, and 15 kV precharge.

Figure 27 documents this charge leakage phenomenon by comparing the total charge of discharges with trigger-times of about 10 and 100 seconds. Fifteen 1mm/s zaps are performed at 10 and 100 mm trigger heights for both 4 and 15 kV. The reduction in total charge due to increased trigger-time is statistically significant per a *t*-test with a significance level of .01. A *t*-test is a statistical measurement of the probability that the means of two datasets are statistically different; for a detailed description, see Appendix B: The *t*-test. The result of this auxiliary study is that trigger-time affects total charge dissipation for discharges of both 4 and 15 kV precharge voltage.
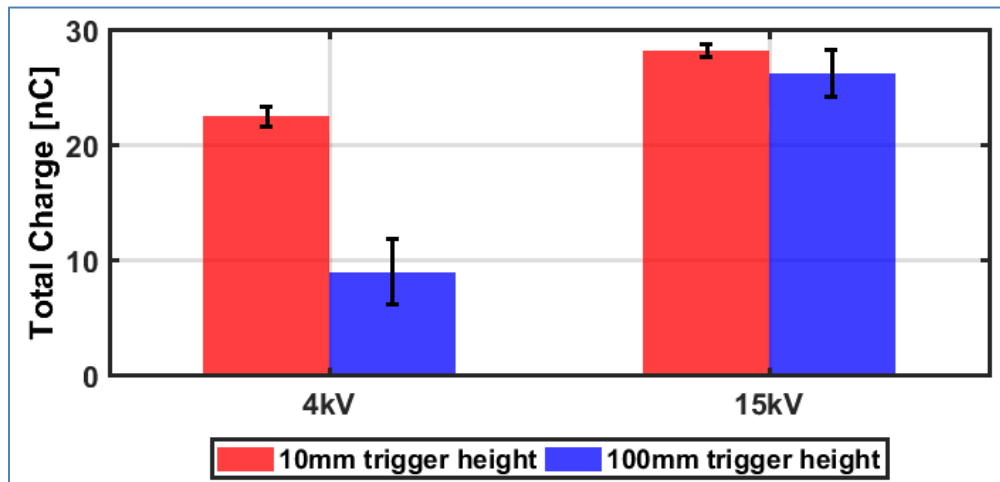
Figure 27. The total charge of discharges from a trigger height of 100mm is less than that of discharges at 10mm because a longer trigger-time correlates to greater charge leakage from the gun's storage capacitor. The approach speed was set at 1 mm/s.

Despite the auxiliary study's demonstrated dependence of total charge on trigger-time, Figure 25 shows that discharges with 4 kV precharge do not exhibit the same trends as those with higher precharge. For precharges of 2 and 4 kV, the trends seen at higher precharge are not present—there is no peak in total charge at 5mm/s and the total charge does not increase above 10 mm/s. It is possible that zaps with lower precharge voltages only experience appreciable leakage in cases of extremely large trigger-time (about 100 seconds); whereas, zaps of 8 kV or higher can see appreciable leakage even with trigger-times of a few seconds. It is also important to note that this auxiliary study's data and the training

dataset were acquired on different days. Room temperature, humidity, and unreliable electrical connections in measurement equipment can affect the discharge waveform; thus, it is recommended that data be taken on a single day. The lack of an appreciable effect from varied trigger-time at low precharge voltage is a topic of further research.

5.3 Rise-Time

Figure 28 shows that rise-time correlates positively with precharge voltage, and for precharges of 4 and 8 kV, rise-time decreases with increasing approach speed. Previous studies have documented a decrease in rise-time with increased approach speed at speeds 50 mm/s and higher.

To explain this phenomenon, studies have shown that spark resistance is correlated with spark length, and both decrease with faster approach speed and increase with greater precharge voltage [4], [7]. It is hypothesized that spark resistance is correlated with rise-time because increased resistance corresponds to a larger RC time constant.

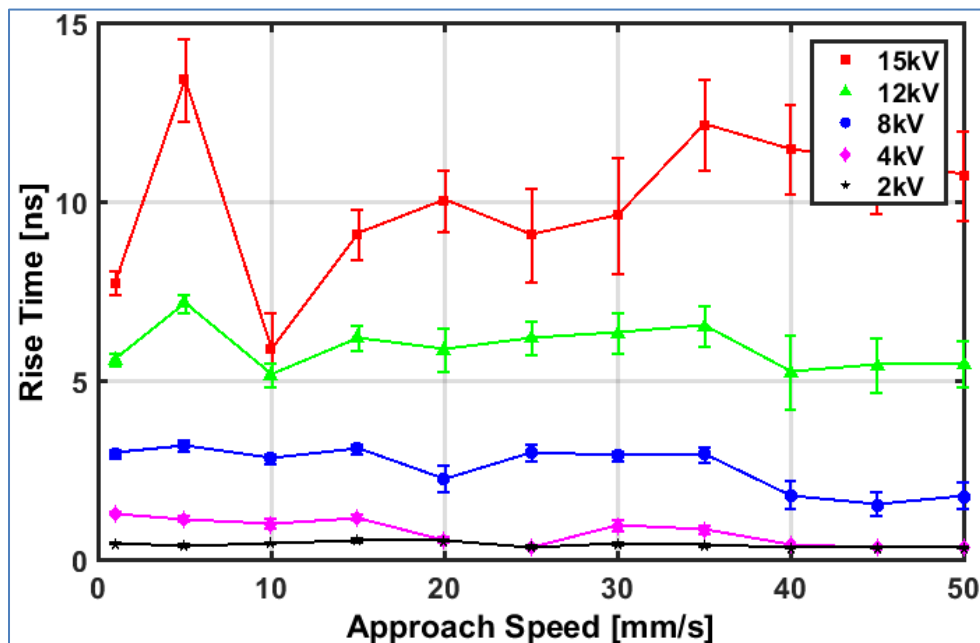Figure 28. Rise-time correlates positively with precharge voltage. At speeds up to 50mm/s, 4 and 8 kV discharges decrease in rise-time with increased approach speed.

Previous studies in [4], [6], and [7] suggest that rise-time should indeed vary inversely with approach speed. However, this trend does not appear for discharges with 2, 12, and 15 kV precharge voltages; nor should it be expected to do so at 2 kV

At 2 kV, no discernable spark forms during approach; rather, the discharge likely occurs through a minute spark gap that is imperceptible to the naked eye. Increased approach speed raises the air pressure in the spark gap and decreases the rise-time of the discharge [7]; however, when the air gap is minute, as in the 2 kV case, rise-time should be effectively insensitive to changes in approach speed.

At approach speeds up to 50 mm/s, it appears that discharges of 12 and 15 kV do not experience a decrease in rise-time. Since prior works investigate exclusively higher speeds, it is unclear whether or not these results are expected.

5.4 Secondary Discharges

Recall that the experiments in this study were designed such that only the first discharge is recorded. At precharge voltages of 4 kV or higher, multiple discharges occur between the gun electrode and EUT during the gun's approach. After the primary discharge, the voltage at the gun tip will have decreased. As the gun continues towards the EUT after the first discharge, the electric field between the tip and EUT will increase until it causes another spark to form.

Secondary discharges can be captured by adjusting the holdoff setting of the oscilloscope to reject the primary discharge. They are most easily captured at low approach speed and high precharge, and the following discharges are performed with 15 kV precharge voltage and 2 mm/s approach speed into a 2 Ω target. Primary and secondary waveforms can differ considerably, as demonstrated in Figure 29.
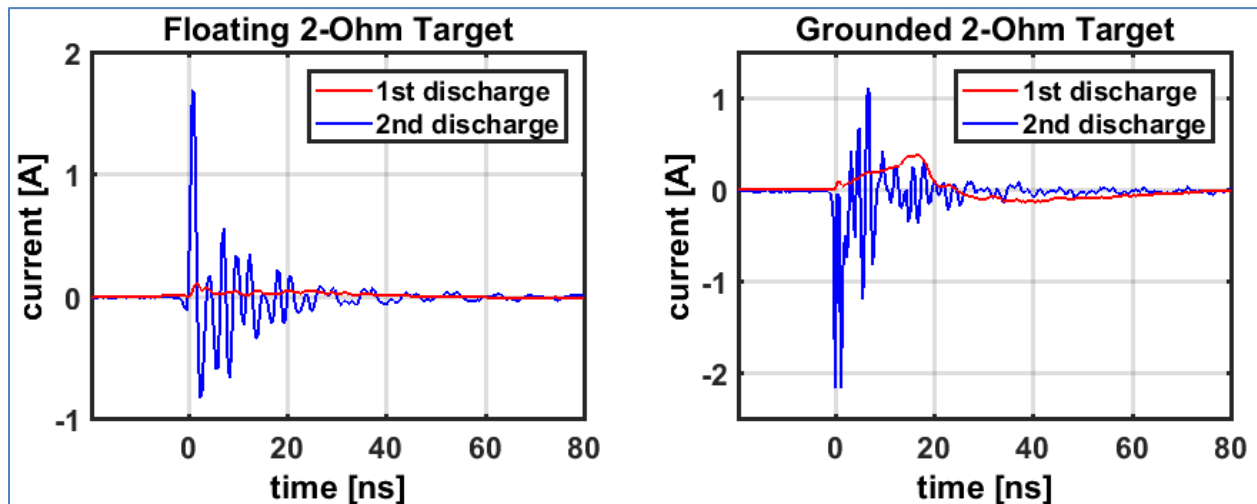

Figure 29. Primary and secondary discharges differ considerably. For a 2 Ω target, the discharge characteristics are presented for both a grounded and floating configuration. Note that the 1st and 2nd discharges do not occur simultaneously but are overlaid on the same time axis. The precharge voltage is 15 kV, and the approach speed is 2 mm/s.

In a grounded configuration, the target is a small resistive load; however, in a floating configuration, the target is capacitive. Per Figure 30, the total charge of a 1st discharge to a grounded EUT is greater than the total charge discharged to a floating EUT. This is due to charge sharing between the gun's storage capacitor and the EUT in the floating configuration. The total charge of secondary discharges is appreciable and can be either positive or negative (with negative charge denoting net current into the gun from the EUT). It is recommended that further experiments be performed to elucidate the physical mechanism for the negative current seen in the grounded case.
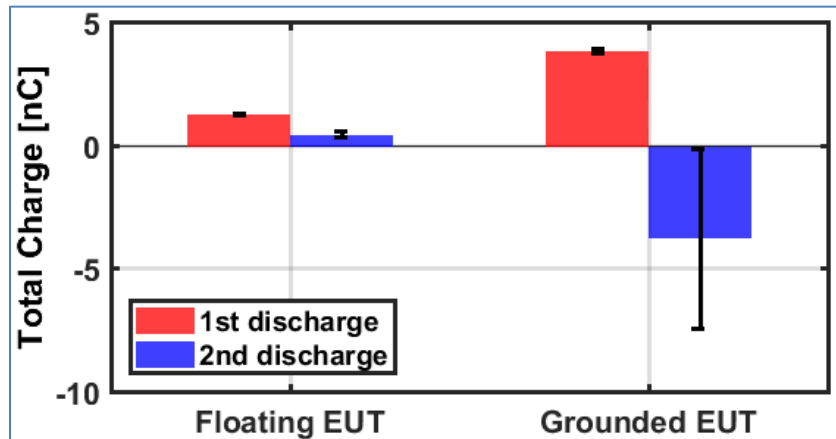

Figure 30. The total charge of a primary discharge to a grounded EUT is greater than that of a floating EUT. The total charge of the secondary discharge can be significant and even negative.

6. Modeling Using Machine Learning

Machine Learning is used to predict the peak current, total charge, and rise-time of a discharge when given the precharge voltage and approach speed. The inherent variability of air discharge lends itself to *generative modeling*—a technique that predicts an output distribution rather than a discrete output value. The naïve Bayes algorithm is a generative modeling technique based on Bayes' theorem, shown in equation (6.1).

$$P(A|B) = \frac{P(B|A)P(A)}{P(B)} \tag{6.1}$$

6.1 Naïve Bayes

The inputs (precharge and approach speed) to the machine learning algorithm are known as *features*; the outputs (peak current, total charge, and rise-time), *variables*.

$$x_i \sim feature\ i\ of\ feature\ vector\ \bar{x}$$
$$y_i \sim variable\ i\ of\ variable\ vector\ \bar{y} \tag{6.2}$$

The naïve Bayes algorithm is an example of classical Bayesian regression in which a *posterior* distribution is derived from *prior* and *likelihood* distributions. The posterior, $P(\bar{y}|\bar{x})$, is the distribution of the variables, given a fixed set of features. The prior, $P(\bar{y})$, is the distribution of the variables over the complete dataset, agnostic of the features associated with each. The likelihood, $P(\bar{x} = \bar{C}|\bar{y})$, is the probability of a certain feature set $\bar{C}$, given the range of variables. Equation (6.3) demonstrates a complete and rigorous formulation of the naïve Bayes model.

$$P(\bar{y}|\bar{x}) = \frac{P(\bar{y}) \prod_i P_i(x_i = C_i|\bar{y})}{P(\bar{x})} \tag{6.3}$$

The product of conditionals over each feature represents the core assumption of the naïve Bayes method. The algorithm assumes that each feature is conditionally independent, and thus equation (6.4) holds. This simplifies the algorithm and provides reliable prediction in most cases, even when the features are not conditionally independent [11].

$$\prod_i P_i(x_i = C_i|\bar{y}) = P(\bar{x} = \bar{C}|\bar{y}) \tag{6.4}$$

The measurement data were obtained at discrete values of precharge voltages and approach speeds. Since both are continuously valued, the derived pdf must be smoothed. Kernel density estimation (KDE) is employed for that purpose [12]. Figure 31 provides the algorithmic implementation of naïve Bayes modeling.

$$P(\bar{y}) \sim KDE(\bar{y})$$

$$P_{temp} = P(\bar{y})$$

$for\ i = 1:k,\qquad where\ k\ is\ the\ number\ of\ features$

$$P(x_i, \bar{y}) \sim KDE([x_i\ \bar{y}])$$

$$P(x_i|\bar{y}) = \frac{P(x_i, \bar{y})}{P(\bar{y})}$$

$$P_{temp} = P_{temp}P(x_i|\bar{y})$$

end

$$P(\bar{y}|\bar{x}) = \frac{P_{temp}}{\int P_{temp}dy},\qquad because \int P_{temp}dy = P(\bar{x})$$

Figure 31. Algorithm for implementation of naïve Bayes for regression

KDE is a common procedure for data smoothing. A kernel is a continuous function, and KDE consists of summing kernels to smooth discrete data. While multivariate KDE is used in this work, equation (6.5) illustrates the technique for solely the i_{th} *variate*. In this work, a variate is a variable or feature that makes up one of the dimensions of the KDE. $P(z_i)$ gives the value of the kernel density estimate at a point z_i of the i_{th} variate using kernel function $K(\cdot)$ [13]. The *kernel bandwidth* for the i_{th} variate is h_i, and the N datapoints for the i_{th} variate are $\left\{z_i^{(1)}, z_i^{(2)}, \dots, z_i^{(N)}\right\}$.

$$P(z_i) = \frac{1}{Nh_i}\sum_{n=1}^{N} K\left(\frac{z_i - z_i^{(n)}}{h_i}\right) \qquad (6.5)$$

In this work, the kernel function $K(\cdot)$ in (6.5) is a normal Gaussian. For normal kernels, the kernel bandwidth is equivalent to the standard deviation of the Gaussian. The kernel bandwidth is given by Silverman's rule of thumb. For the i_{th} variate of a KDE with d-variates, Silverman's bandwidth h_i is given by equation 6.6 [14]. In calculating the prior, $P(\bar{y})$, the KDE is three-dimensional, and in calculating the likelihood, $P(\bar{x} = \bar{C}|\bar{y})$, the KDE is four-dimensional.

$$h_i = \sigma_i\left(\frac{4}{(d+2)N}\right)^{\frac{1}{d+4}} \qquad (6.6)$$

6.2 Posteriori Post-processing

Post-processing of the posterior incorporates physical intuition into the model. Peak current, total charge, and rise-time are always positive values for primary discharges. The posterior is modified such that the probability of a negative value for any of the variables is zero. The posterior is re-normalized to

preserve the property of joint pdfs that it integrates to unity. Note that this post-processing is performed after the posterior is generated, so non-physical negative values may be assigned non-zero probability during intermediate steps of the naïve Bayes algorithm.

6.3 Example Test Case

This section presents the generation of a model and a prediction of the output variables given a set of features. The features of this test case are a 12 kV precharge voltage and 40 mm/s approach speed. This test feature set is denoted mathematically as $\bar{C} = \{12, 40\}$.

Figure 32 plots the subset of the training dataset for peak current, y_1, and three overlaid marginal pdfs. The algorithm produces multivariate pdfs over all of the variables; however, to generate the plots in this section, two of the three variables are integrated out to produce marginal pdfs that only include one variable. Precharge levels are represented as distinct markers, and approach speed is on the left vertical axis. The first pdf is the marginal $P(y_1)$ of the prior $P(\bar{y})$. The second and third pdfs are marginals $P(y_1, x_1)$ and $P(y_1, x_2)$ evaluated at $\bar{x} = \bar{C}$ of joint pdfs $P(\bar{y}, x_1)$ and $P(\bar{y}, x_2)$. These two marginals are normalized for readability; this normalization causes them to be mathematically equivalent to conditional pdfs $P(y_1|x_1 = C_1)$ and $P(y_1|x_2 = C_2)$. Figure 33 presents the dataset and pdfs for total charge, y_2; and Figure 34, for rise-time, y_3.
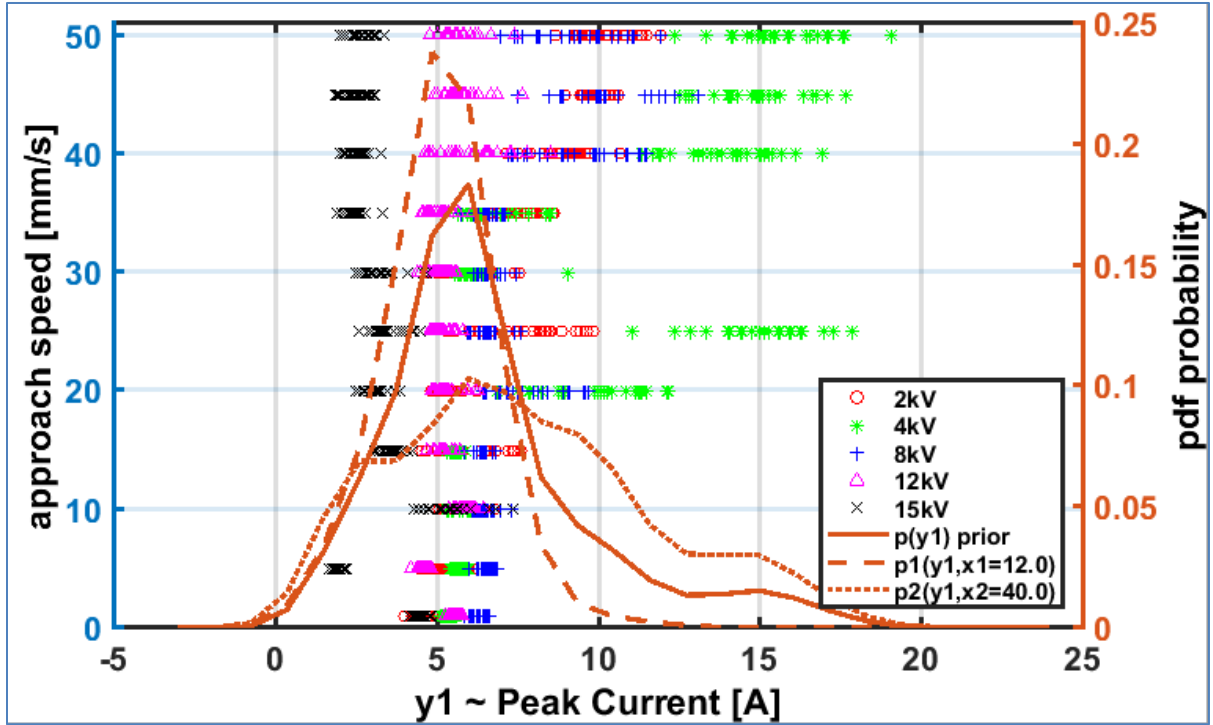
Figure 32. Peak current dataset and marginal pdfs for the 12 kV, 40 mm/s test case. Marginals are normalized for improved readability. This normalization of p1 and p2 makes the pdfs equivalent to conditional pdfs $p_1(y_1|x_1 = 12.0)$ and $p_2(y_1|x_2 = 40.0)$, respectively.
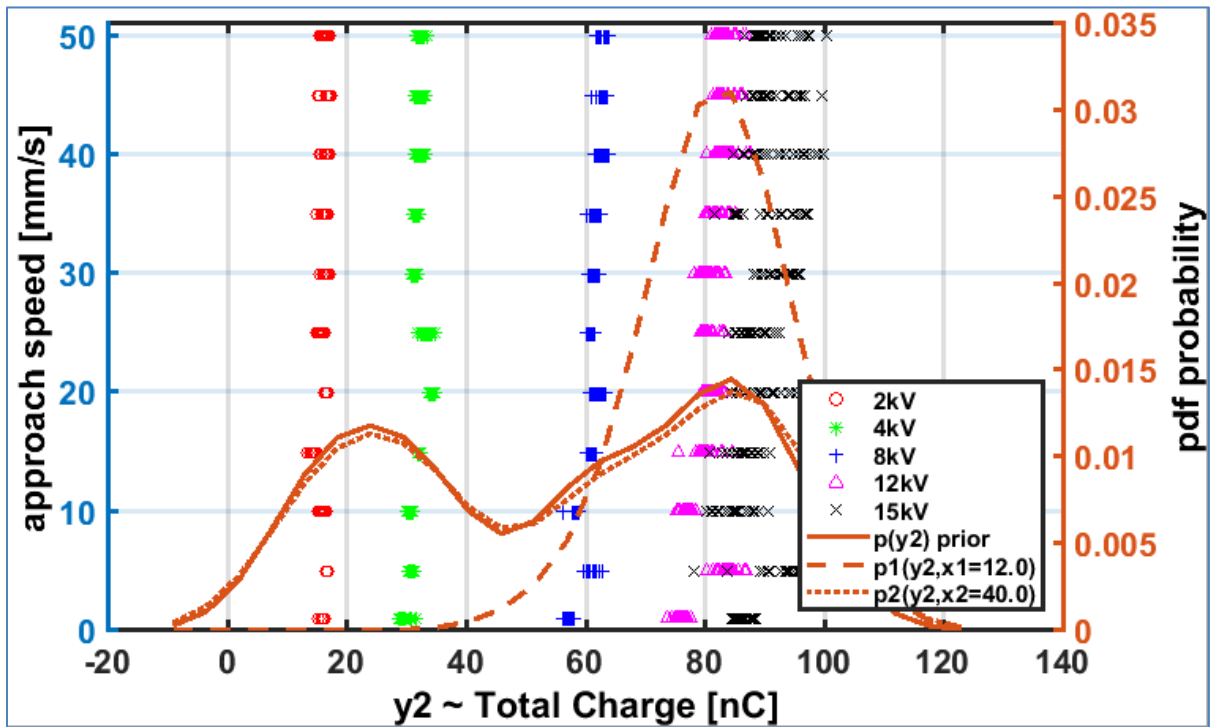

Figure 33. Total charge dataset and marginal pdfs for the 12 kV, 40 mm/s test case. Marginals are normalized for improved readability. This normalization of p1 and p2 makes the pdfs equivalent to conditional pdfs $p_1(y_1|x_1 = 12.0)$ and $p_2(y_1|x_2 = 40.0)$, respectively.
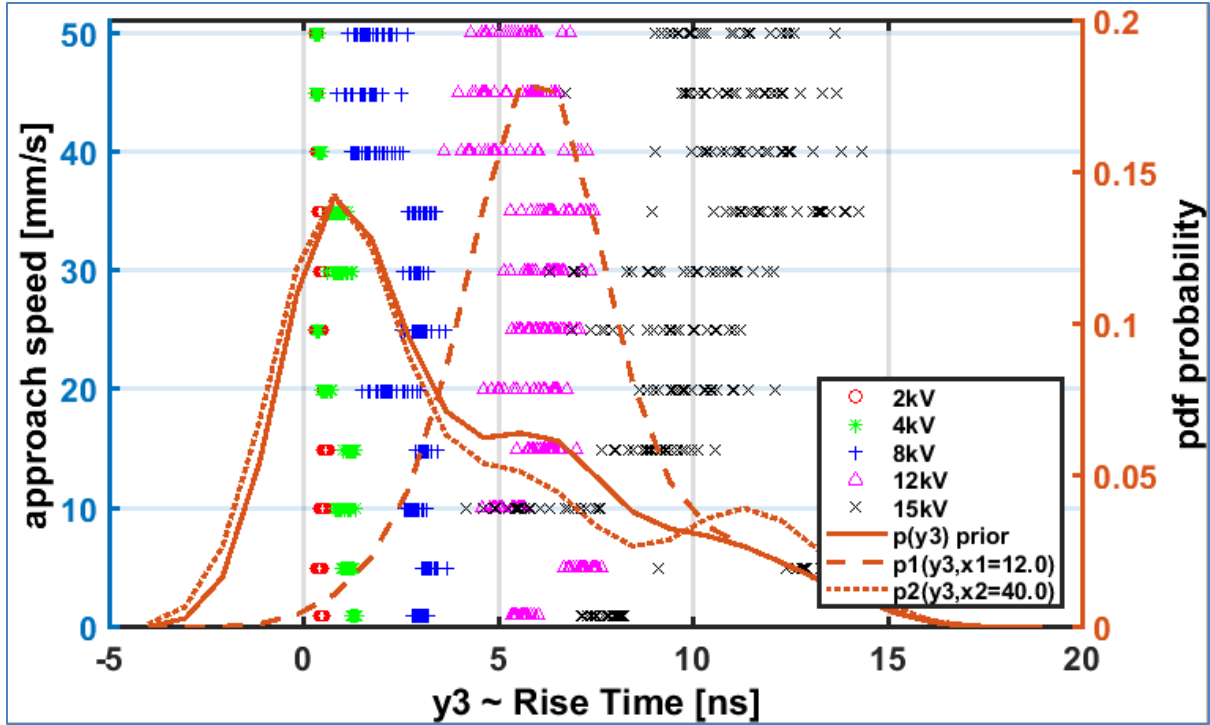
Figure 34. **Rise-time dataset and marginal pdfs for the 12 kV, 40 mm/s test case. Marginals are normalized for improved readability. This normalization of p1 and p2 makes the pdfs equivalent to conditional pdfs** $p_1(y_1|x_1 = 12.0)$ **and** $p_2(y_1|x_2 = 40.0)$**, respectively.**

The naïve Bayes algorithm produces a posterior conditional pdf, $P(\bar{y}|\bar{x})$, of the output variables given the input features. Figure 35, Figure 36, and Figure 37 display this posterior as marginal pdfs $P(y_i|\bar{x})$ for each output variable. The posterior pdf is shown in blue with the expected value and standard deviation overlaid. The histogram is derived by sampling from the posterior using the Metropolis-Hastings algorithm described in Section 7.1. The histogram is normalized by dividing the number of samples in each bin by to the total number of samples.

Figure 35. The peak-current marginal of the posterior distribution, given features of 12 kV precharge and 40 mm/s approach speed, is plotted in blue. The posterior is sampled and a normalized histogram of the peak currents of these samples is overlaid.

Figure 36. The total-charge marginal of the posterior distribution, given features of 12 kV precharge and 40 mm/s approach speed, is plotted in blue. The posterior is sampled and a normalized histogram of the total charge of these samples is overlaid.

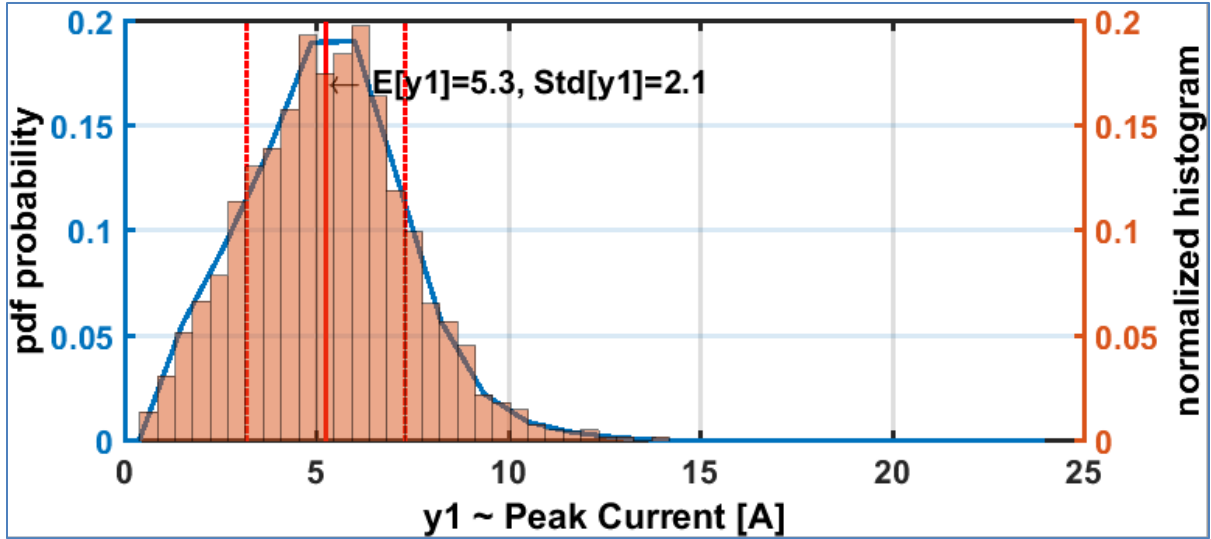**Figure 37.** The rise-time marginal of the posterior distribution, given features of 12 kV precharge and 40 mm/s approach speed, is plotted in blue. The posterior is sampled and a normalized histogram of the rise-times of these samples is overlaid.
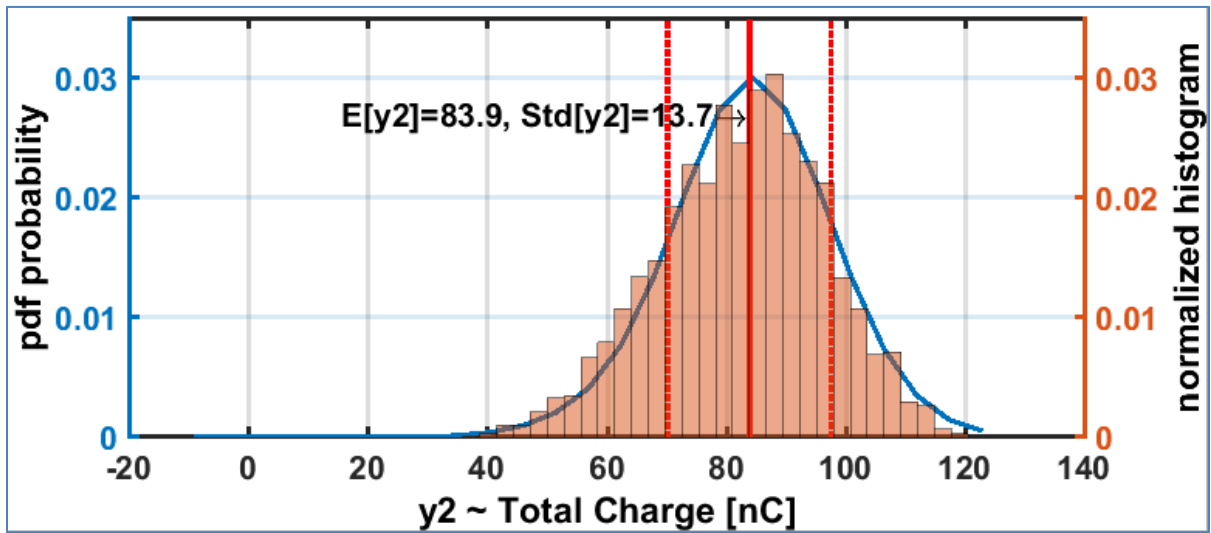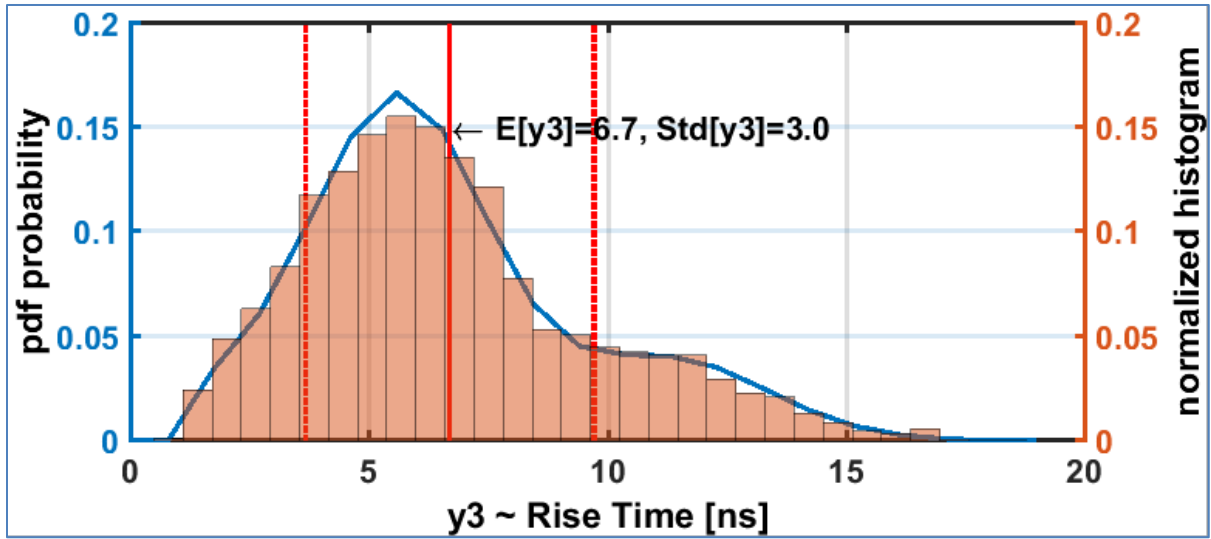
7. Validation

The model is validated by comparing predicted posteriori to measurement data. The measured validation data was not included in the training dataset. The validation dataset consists of 100 discharges at each of the four following sets of feature: 12 kV, 40 mm/s; 10 kV, 40 mm/s; 8 kV, 27.5 mm/s; 3 kV, 27.5 mm/s.

7.1 Sampling Posteriori

Sampling from an arbitrary posterior distribution is best accomplished using Markov Chain Monte Carlo methods [15]. The Metropolis-Hastings algorithm is applied in three-dimensions to sample the posterior. Figure 35, Figure 36, and Figure 37 demonstrate the accuracy of this sampling method since the histogram distributions of posterior samples are comparable to the marginal pdfs of the posterior.

A Markov chain is a random process that generates a sequence of states, where the next state is solely a random function of the current state. In the context of this algorithm, a state is a set of one peak current value, one total charge value, and one rise-time value. The Metropolis-Hastings algorithm builds a Markov chain by first sampling a *candidate* state from a *proposal function* centered on the previous state; next, the algorithm either iterates on the previous state or the candidate based on their relative probability, per the posterior.

In this work, the proposal function used to generate a candidate state is a set of three independent Gaussian normal distributions—one for each output variable. For each variable, the mean of the Gaussian proposal function is set to the value of that variable in the previous state. The standard deviation of the proposal function affects the rate at which the algorithm traverses the support of the posterior. The presented samples were obtained by setting the standard deviation of each variable's respective Gaussian to the standard deviation of the posterior marginal pdf for that variable.

Figure 38 presents the algorithm for implementation of Metropolis-Hastings sampling. $\pi(\cdot)$ denotes the value of the posterior at a given state.

$Initialize\ \bar{y}^{(0)} \sim N(\bar{\mu}, \bar{\sigma})$

$for\ i = 1, 2, \ldots, n$

$\quad propose\ \bar{y}^{cand} \sim N(\bar{y}^{(i-1)}, \bar{\sigma});$

$\quad \alpha = min\left\{1, \dfrac{\boldsymbol{\pi}(\bar{y}^{cand})}{\boldsymbol{\pi}(\bar{y}^{(i-1)})}\right\}$

$\quad \bar{y}^{(i)} = \begin{cases} \bar{y}^{cand},\ with\ probability\ \alpha \\ \bar{y}^{(i-1)},\ with\ probability\ 1 - \alpha \end{cases}$

end

Figure 38. Implementation of the Metropolis-Hastings algorithm for indirect sampling of a pdf

7.2 Validation Results

In order to validate the model, posterior samples are compared to measured validation data, given the same input features. Normalized histograms of the validation data and posterior samples are generated over identical bins. Note that these bins are 3-dimensional since they each contain a range of peak currents, total charges, and rise-times. The root-mean-square-error (RMSE) between the normalized values in each histogram over every bin provides a metric for prediction error. Essentially, the RMSE value gives the percentage by which the prediction and measurement differ by averaging the difference over each bin. A lower RMSE corresponds to a better prediction. Equation 7.1 defines the RMSE in mathematical detail with B as the total number of bins.

$$RMSE = \sqrt{\frac{1}{B}\sum_{i=1}^{B}\left(h_{samp}^{(i)} - h_{meas}^{(i)}\right)^2} \tag{7.1}$$

The results in Table 2 demonstrate strong predictive ability of the model. The predictive ability decreases slightly as the validation features stray from the training dataset. The 12 kV, 40 mm/s test case demonstrates the smallest error (or best prediction), and that set of features was part of the training dataset. The 3 kV, 27.5 mm/s test case has the largest error (or worst prediction), and neither of those values for features were included in the training data. The other two test cases have one of two features in common with the training dataset, and they demonstrated error between that of the two extreme cases.

Table 2. Validation results

Precharge [kV]	Approach Speed [mm/s]	RMSE [%]
12	40	1.29
10	40	1.50
8	27.5	1.59
3	27.5	2.75

8. Conclusion and Future Work

An automated ESD test system provides repeatable air discharge data on an IEC 16000-4-2 compliant testbed. Measured data is used to analyze the effects of approach speed on air discharge and produce accurate models.

Previous works performed at speed greater than 50 mm/s claim that peak current correlates positively, and rise-time correlates negatively, with approach speed. At speeds up to 50 mm/s, this work corroborates that finding for discharges with precharge voltages of 2, 4, and 8 kV; however, discharges at precharges of 12 and 15 kV do not exhibit an appreciable correlation to these approach speeds. Future work should seek to identify if a threshold approach speed exists at which discharges of higher precharges begin to be affected by variations in approach speed.

A methodology for applying machine learning to ESD modeling is presented. The naïve Bayes method proves to be an effective statistical learning method for modeling air discharge ESD. It predicts physically intuitive posterior distributions and validates well against validation data.

The automation system and accompanying analysis codebase lay the foundation for future work in air discharge and statistical modeling. Future work in data preprocessing should aim to identify a solution for de-embedding the current probe's DC block characteristic. To gain further insight into this statistical learning method, it would be pertinent to study the effect of using a sparser or smaller training dataset. Understanding the quantity of data needed to produce an effective model is important when making the case for using statistical learning methods in electronics modeling. Additional features such as trigger-time, EUT area, and EUT elevation over the horizontal coupling plane should be added to the model. Further, the configuration of the EUT could be varied by grounding the EUT instead of connecting it to the HCP through the IEC standard 940 MΩ bleed-off resistance. It is hypothesized that peak current, total charge, and rise-time are correlated to ESD-induced soft or hard failures; however, this work could be extended to predict additional variables or entire waveforms. The correlation between discharge parameters and ESD-induced failures should be studied experimentally.

Appendix A: The IEC Testbed

The International Standard IEC 16000-4-2 ESD testbed is diagramed in Figure 39. The testbed consists of a table with a conducting horizontal coupling plane (HCP) on top of it and a ground plane below it. The table and conducting planes have prescribed dimensions defined in the standard. The EUT rests on an insulating sheet on the HCP.
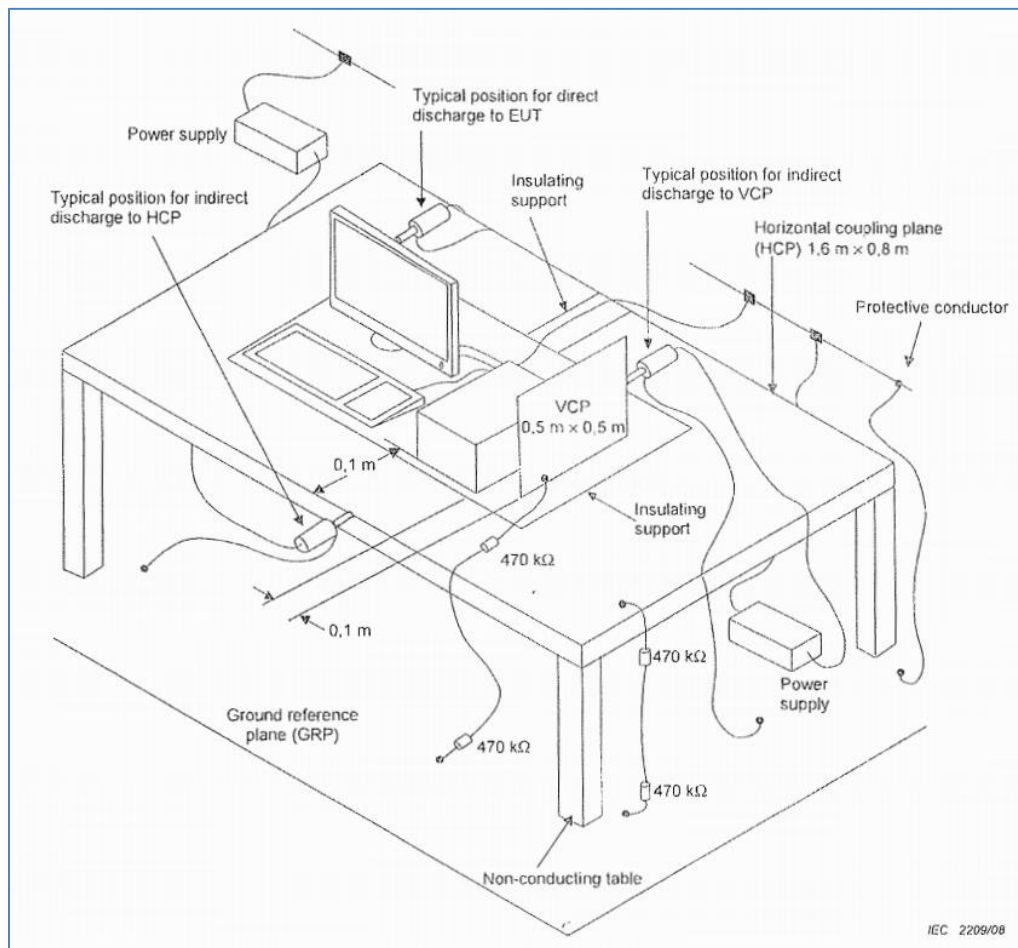

Figure 39. IEC 16000-4-2 standard testbed from [3]

Appendix B: The *t*-test

The *t*-test is a mathematical procedure for determining statistical significance. The test determines whether the means μ_X and μ_Y of two datasets X and Y with standard deviations σ_X and σ_Y and number of observations N are *statistically* different. The *null hypothesis* is that the datasets are not statistically different, given a significance level α.

A *t*-statistic (t_{stat}) is calculated for the given data, and a critical *t*-value (t_{crit}) is calculated for only N and α. If $|t_{stat}| < t_{crit}$, the null hypothesis holds.

The *t*-statistic is analogous to a signal-to-noise-ratio and is given by the difference in means divided by the standard error of the difference [16].

$$t_{stat} = \frac{\mu_X - \mu_Y}{\frac{1}{\sqrt{N}}(\sigma_X + \sigma_Y)}$$

The *t*-distribution is a pdf based solely on N and is composed of gamma (Γ) functions [17]. Note that this is an even function.

$$f_N(t) = \frac{\Gamma\left[\frac{1}{2}(N+1)\right]}{\sqrt{N\pi}\,\Gamma\left(\frac{1}{2}N\right)\left(1+\frac{t^2}{N}\right)^{\frac{N+1}{2}}}$$

t_{crit} is defined such that $P(t < -t_{crit} \text{ or } t_{crit} < t) = \alpha$, as shown in Figure 40 [18]. If $|t_{stat}| < t_{crit}$, then the null hypothesis holds for the given significance level. However, if $|t_{stat}| > t_{crit}$, the means of the two distributions are indeed statistically different for the given significance level.
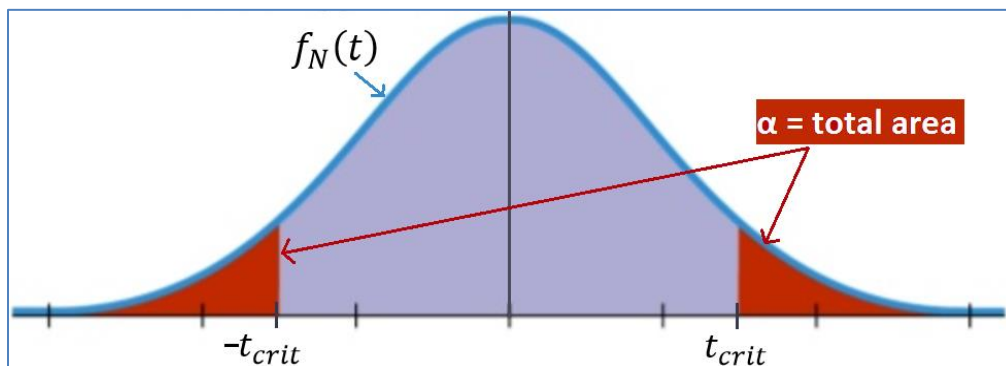

Figure 40. If the *t*-statistic lies in the red regions, the null hypothesis is false, and the means of the distributions being compared are statistically different. Image based on [19].

References

[1] T. Ishida, F. Xiao, Y. Kami, O. Fujiwara and S. Nitta, "An alternative air discharge test in contact discharge of ESD generator through fixed gap," in *International Symposium on Electromagnetic Compatibility*, Ottawa, ON, Canada, 2016.

[2] H.-M. Ritter, L. Koch, M. Schneider and G. Notermans, "Air-discharge testing of single components," in *Electrical Overstress/Electrostatic Discharge Symposium (EOS/ESD)*, Reno, NV, USA, 2015.

[3] NSAI Standards, *Electromagnetic compatibility (EMC) -- Part 4-2: Testing and measurement techniques - Electrostatic discharge immunity test (IEC 61000-4-2:2008 (EQV)),* 2009.

[4] Y. Taka, K. Kawamata and O. Fujiwara, "Dependence of grounded metal-plate's approach speed on spark length for air discharges of electrostatic discharge generator," in *Asia-Pacific Symposium on Electromagnetic Compatibility (APEMC)*, Taipei, 2015.

[5] F. Ruan, W. Zhu, G. Li and X. Yang, "Investigation of low repeatability in parameters measurement of non-conducted electrostatic discharge," in *International Symposium on Electromagnetic Compatibility*, Gothenburg, 2014.

[6] K. Fujita, J. Zhou and D. Pommerenke, "Hybrid full-wave/circuit modelling of spark gaps and its experimental validation," *Electronics Letters,* vol. 53, no. 7, pp. 484-486, 2017.

[7] F. Ruan, D. Shi, F. Zhou, Y. Gao and R. Linghu, "Analysis of air pressure reduction caused by electrode speed in short gap electrostatic discharge (ESD)," in *Zurich Symposium on Electromagnetic Compatibility*, Zurich, Switzerland, 2009.

[8] X. Xiaoying, L. Qiongli, L. Qingrong and W. Dinghu, "Study on the relation of electrostatic discharge parameters," in *International Conference on Electronic Measurement and Instruments*, Xi'an, China, 2007.

[9] T. Ishida, S. Nitta, F. Xiao, Y. Kami and O. Fujiwara, "An experimental study of electrostatic discharge immunity testing for wearable devices," in *IEEE International Symposium on Electromagnetic Compatibility*, Dresden, Germany, 2015.

[10] T. Ishida, Y. Tozawa, M. Takahashi, O. Fujiwara and S. Nitta, "A measurement on electromagnetic noises from ESD generator just before and after ESD testing," in *IEEE Symposium on Electromagnetic Compatibility*, Tokyo, 2014.

[11] K. P. Murphy, *Machine Learning: A Probabilistic Perspective*, Cambridge, MA: MIT Press, 2012.

[12] B. Scholkopf and A. J. Smola, *Learning with Kernels*, Cambridge: MIT Press, 2002.

[13] S. J. Sheather, "Density Estimation," *Statistical Science,* vol. 19, no. 4, pp. 588-597, 2004.

[14] MathWorks, "mvksdensity," [Online]. Available: https://www.mathworks.com/help/stats/mvksdensity.html. [Accessed 26 June 2017].

[15] C. Andrieu, N. De Freitas, A. Doucet and M. I. Jordan, "An Introduction to MCMC for Machine Learning," *Machine Learning,* no. 50, pp. 5-43, 2003.

[16] W. Trochim, "Web Center for Social Research Methods," 20 October 2016. [Online]. Available: https://www.socialresearchmethods.net/kb/stat_t.php. [Accessed 24 June 2017].

[17] E. Weisstein, "Students' t-Distribution," [Online]. Available: http://mathworld.wolfram.com/Studentst-Distribution.html. [Accessed 24 June 2017].

[18] Pennsylvania State University, "3.2 - Hypothesis Testing (P-value approach)," 2017. [Online]. Available: https://onlinecourses.science.psu.edu/statprogram/node/138. [Accessed 24 June 2017].

[19] calculistictt, "Chapter 20 and 21 combined testing hypotheses about proportions 2013," 20 November 2013. [Online]. Available: https://www.slideshare.net/calculistictt/chapter-20-and-21-combined-testing-hypotheses-about-proportions-2013. [Accessed 24 June 2017].